UNIVERSIDAD CARLOS III DE MADRID
ESCUELA POLITÉCNICA SUPERIOR

DEVELOPMENT OF AN UNSTEADY POTENTIAL MODEL FOR A FLAPPING WING MAV

Bachelor Thesis

Author
Gonzalo Arranz Fernández

Leganés, September 2015

Department of Aerospace Engineering
ESCUELA POLITÉCNICA SUPERIOR

DEVELOPMENT OF AN UNSTEADY POTENTIAL MODEL FOR A FLAPPING WING MAV

Bachelor in Aerospace Engineering

Author
Gonzalo Arranz Fernández

Supervisor
Óscar Flores Arias

Leganés, September 2015

Acknowledgements

I would like to express my gratitude to my professor, Óscar, for his continuous guidance and support from the beginning and throughout this project. This project would not have been possible without his attention. I would also like to thank the Aerospace Engineering department, it has been a pleasure to work there and learn new things every day.

I would also like to thank Blanca. We have had to spend a lot of time together, and working on this project would not have been the same without you.

Of course, a big thank you to my family, for their continuous support, not only with this project, but in everything. And thanks to Irene, for bringing some order to this mess I am.

Contents

List of Figures

Chapter 1

Introduction and Motivation

Human beings have always tried to mimic Nature. This enthusiasm has been the source of many of the most relevant advancements in science throughout History. Moreover, these advances have fostered the development of further advancements and new technologies that have eased somehow human beings' lives.

In this frame, one of the most extraordinary features of Nature that scientists and engineers of all times have always tried to reproduce is the animal flight. Originally -before manned flight-, this fascination for natural flyers, specially for birds, was originated by the desire of flying. However, after more than a century since humankind conquered the skies, the flight of animals calls the attention of the scientific world for other reasons. This interest comes from the birds' and insects' ability to fly in an extremely efficient way, as compared to man-made flying machines built until now. Just to give an overall idea of this fact, Ref. [1] provides several figures of merit. For example, the SR-71 'BlackBird' flying at supersonic speeds near Mach 3, travels about 32 times its body length per second; on the other hand, a typical flight velocity of a pigeon is around 22.4 m/s, which entails it covers around 75 body lengths per second. Similarly, acrobatic aircraft can roll at a rate of 720°/s, whereas a Barn Swallow can have roll rates greater than $5,000$°/s.

In view of the above, it is not surprising that the engineering community has focused on research and development of the so-called, micro air vehicles (MAV).

1.1 Micro Aerial Vehicles: State of the Art review

Although there is no approved definition by any certification authority, MAV is commonly defined (see [1], [2] and [3]) as a *small and ultra-lightweight air vehicle system with a maximum wingspan of 15 cm.*

1.1.1 Applications

Due to their dimensions, MAVs would be able to perform a wide range of missions [3]. For example, MAV are very suitable for reconnaissance and surveillance missions in hazardous environments for human beings. In this fashion, MAV could help search survivors in rescue missions, as those produced in terrorist attacks or natural disasters. Likewise, they could be used for biochemical sensing by flying inside a contaminated environment. Moreover, these kind of systems can be useful for completely different applications as urban traffic management or pipeline inspections; in fact, quad drones are being used for this in pilot projects.

Previous examples are only a few of the numerous applications that MAV could perform, and they give an idea of the enormous impact MAVs will have in the future.

1.1.2 Successful Projects

In view of the potential of MAV, it is remarkable that the number of successful MAV is very reduced. This is due, in part, to the small weight these systems have. The inclusion of all the elements these vehicles require for their functioning entails an important challenge in terms of miniaturization [4]. Fortunately, the progress in miniaturization of sensors, processing devices and power plants; and the advancement in material technologies, has allowed several groups have successfully designed and developed different MAV [1]. To cite some examples, the Harvard School of Engineering and Applied Science and the Wyss Institute developed successfully an insect-scale robot, named as RoboBee (Figure 1.1a), with a mass of 80 mg and a wingspan of 3 cm. AeroVironment developed in 2011, under a DARPA (Defense Advanced Research Projects Agency) sponsored research contract, a hummingbird-like flapping wing design , which is shown in Figure 1.1b. Another outstanding MAV development is that carried out by the Delft university; which recently developed a flapping wing MAV, named as Delfly Explorer

(Figure 1.1c), that can perform autonomous flight with a mass of 20 g. Further details of these projects can be found in [5], [6] and [4], respectively.

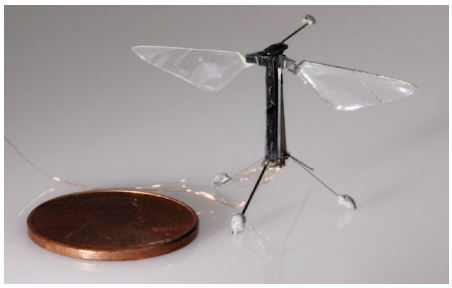

(a) Robobee

(b) Nano Hummingbird

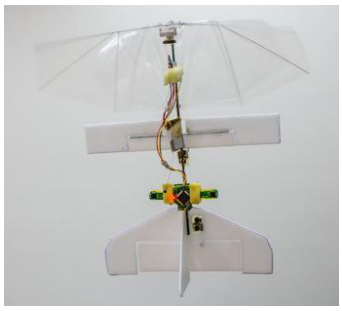

(c) Delfly Explorer

Figure 1.1: Examples of successful MAV developments. Sources: wyss.harvard.edu, www.avinc.com/nano and www.delfly.nl/explorer.

1.1.3 Challenges

Although previous projects have demonstrated to be able to fly, current development of MAV is still far away from exploiting to the fullest the potential of these kind of systems. In fact, there are several fields where a huge research process will be required to overcome the current limitations MAV developments are facing.

Autonomous Flight

The limited autonomy of these systems is one of the challenges engineers are dealing with nowadays. Due to the limited payload MAV can carry, the number and size of batteries and external systems are very limited. Therefore, the kind of batteries that can be installed on a MAV allows it to flight only for a few minutes.

Also related to the autonomy, is the design of a MAV capable of performing autonomous flight. In this regard, there are different challenges depending on the level of autonomous flight.

Tailless MAV are inherently unstable; therefore, for this kind of MAV, it is necessary the implementation of an active attitude stabilization software that continuously stabilize the vehicle [4]. The *nano Hummingbird* first achieve it with onboard sensing and processing devices.

Another issue is the automatic obstacle avoidance. Although the *Delfly Explorer* is capable of avoiding obstacles in a generic environment, there are still many obstacles to be overcome in order to design a fully autonomous MAV that can fly in any environment.

Aerodynamics

As it was stated above, flapping wings significantly enhance the manoeuvrability of a flying device as compared to a wing-fixed vehicle. However, the physics of flapping wings based systems is much more complex than that of a fixed wing aerial vehicle. Whereas an airplane with a fixed wing configuration produces lift thanks to an incoming velocity, and thrust with the engines; birds and insects move their wings to produce lift and thrust at the same time, accordingly to the flight circumstance. To accomplish that, natural flyers do not only flaps their wings up and down, but they also plunge and sweep. In turn, they combine their wings' flapping motion with wing deformation, body contour, and tail adjustments to further improve flying manoeuvres [1]. Consequently, the analysis of animal flight is much more complex than the analysis of fixed wing machines, as can be the case of an aircraft. Some of the difficulties that arise when analysing animal flight are explained below.

First of all, it is necessary to define the actual motion of a flying animal. However, taking into account that the flapping frequency of a hummingbird is around 23 Hz [7], and small insects flaps their wings at frequencies of 200 Hz and 150 Hz -the *Drasophila melanogaster* [8] and the *bombus terrestris* [9], respectively-, a full characterization of the wings' motion is not a straightforward task. Fortunately, recent advances in videography, such as high-speed videocameras; and in flow visualization, such as particle image velocimetry (PIV) technology, have enabled scientists to achieve a better understanding of the animal's flapping mechanism, as well as the behaviour of the flow around them [1] [10].

After the characterization of the flapping motion, it is necessary to develop an aerodynamic model that implements such motion in order to determine the aerodynamic forces and the importance of each parameter. However, the required

aerodynamic models are largely different from those used in the aeronautic field. Typical aerodynamic problems deal with fixed wings at an small angles of attack and Reynolds numbers of the order of 10^7. Being the Reynolds number defined as:

$$Re = \frac{\rho U_c l_c}{\mu},$$

where ρ is the fluid density, U_c is the characteristic velocity of the flow, l_c is a characteristic length, and μ is the kinematic viscosity of the flow.

Under these conditions, the flow can be considered steady, the viscous forces negligible, and one can consider the flow remains attached to the wing. On the contrary, MAV operates in the range of Reynolds number from 10 to 10^5 [10]. Therefore, for certain flight configuration, viscous effects may become important. Likewise, wide amplitude movements that are characteristic of flapping wings yields in high angles of attack where it cannot be presumed the flow will remain attached to the wing, and separation of the boundary layer is prone to occur. Furthermore, the oscillatory motion of the wings makes it unable to consider the problem steady. Even for harmonic motion, unsteady effects, such as the interaction of the wing with the wake, must be taken into account. In fact, they represent an important contribution to the aerodynamic forces. A thorough discussion of these effects is found in [1] and [10].

Several aerodynamic models are being used to analyse the aerodynamics of animal flight in order to design efficient MAV systems. On the one hand, there are the quasi-steady models. They are called low order models because they are based on simplified models based on quasi-steady approximations. According to that, the instantaneous forces on a wing are equal to the forces that the same wing produces at the same angle of attack and instantaneous velocity during a steady motion [10] [11]. The advantage of quasi-steady methods is that they are relatively simple and imply very low computational cost. However, by neglecting the time history of the flow, unsteady effects are not considered. Therefore, aerodynamic forces are not accurately predicted.

On the other hand, there are the so-called high order models. These models implement the Navier-Stokes equations to the flow surrounding the flapping wings. By using high-order Navier-Stokes models[1], the aforementioned effects in flapping motion are accounted for, such as the effect the effect of viscosity, unsteady effects, the interaction of the fluid with the wings, and flow separation. In this fashion, high-order models accurately predict the aerodynamic forces as well as the flow behaviour of flapping wings. However, they imply an enormous computational cost and time.

[1]Throughout the document, high-order Navier-Stokes models are often denoted as high-order NS models.

In the middle of these two models are the panel methods; based on unsteady potential flow. Potential flow assumes inviscid, irrotational and incompressible flow. They are very suitable for analysing the aerodynamic performance of streamline shapes such as wings [12]. Therefore, although they cannot lead with flow separation and the effect of viscous forces at very low Re numbers, they can provide accurate results for moderate configurations, yielding to be very efficient in terms of computational time, when compared to high-order Navier-Stokes models.

Therefore, the selection of the aerodynamic model is a trade-off between accuracy and time. When it is desired to analyse a given flight condition with a given geometry, high-order Navier-Stokes models are the best option if an accurate result is desired. However, if one desires to investigate the nature of flapping wing, the computational cost would be unbearable. First of all, there are many different flapping parameters, whose importance must be assessed: the frequency of flapping, pitching and/or sweeping, the amplitude of each movement; the phase among them; the relation between the wing size and the beating frequency; the shape of the wings... Secondly, the interaction among them must also be evaluated. Under this frame, the use of lower-order models such as panel's methods prove to be extremely useful, since they can yield accurate results with low computational cost.

Motivated by the broad-span of the capabilities of these latter models, the aim of this project is the development of an unsteady potential aerodynamic model for a flapping wing MAV. This tool will allow to investigate flapping wing mechanisms, such as asymmetric flapping, or it could be used –due to its low computational cost– as an embedded flight controller.

1.2 Socio-economic and Legal Framework

From the previous discussion about the huge capabilities and possible applications of MAV, it is not surprising UAV market is currently undergoing a great expansion. In fact, according to a research by MarketandMarkets, this market is expected to reach $ 1.27 billion in 2020 [13].

Regarding a legal framework, there exist a regulation in Spain aimed to control activities UAV can perform in the Spanish Airspace. Since the present project is a research project focused on the aerodynamics of flapping wing MAVs, it is not subjected to any regulation, Nonetheless, the current regulation can be found in [14].

Chapter 2

Objectives

The objectives to be achieved in this project can be split into two categories: main and secondary objectives.

Main Objective. The main objective of this project is the development of an unsteady potential code that allows to compute the aerodynamic forces of two wings with an arbitrary motion. The code must be able to reasonably predict aerodynamic forces with a low computational cost and in a fast way. In this fashion, the code will allow, in a future, to analyse different flapping configurations with different parameters, that would be impossible to analyse using high order NS based methods.

Secondary Objectives. To achieve the main objective, a list of secondary objectives follows:

- Literature review. A review of the state of the art of MAV is made (presented in Chapter 1), as well as a review of the existing projects related to numerical methods, both high order methods and unsteady potential methods. Special attention has been paid to the latter, in order to build the numerical code.
- Development of a unsteady potential code for a single wing. In order to develop the main code, a preliminary, simpler version with one wing will be developed.
- Modification of the code to be interfaced with the code developed in [15]. The goal of this joint work is the development of an algorithm to simulate both the aerodynamics and dynamics of a flapping wing MAV. Hence, the present code is transformed into a function whose inputs are velocity, position and

orientation of the MAV that are provided by a dynamic model; its outputs are the aerodynamic forces produced under a prescribed wings' motion. In turn, aerodynamic forces are the inputs of the dynamic model[1].

- Validation of the codes. Several cases are run and compared to existing literature to validate the codes.
- Simulation of heaving and pitching cases. In order to test the capabilities of the code, cases where flow separation is expected and viscous effects are important, are run and compared to experimental results or results from high order models.
- Heaving and Flapping analysis. Different flapping motions are run and the results are analysed and compared amongst them and to those of heaving in order to determine possible efficient flight configurations.

Even though objectives of the present project are those cited above, it must be highlighted that this project is framed within a larger effort, whose final purpose is the development of an efficient and autonomous flapping wing MAV. Within this framework, the unsteady potential code is a tool that will serve to analyse a wide spectrum of different flapping wing configurations in a quick way, evaluating which configuration is better. Thus, the best configuration can be analysed in detail by a high order model. Besides, after simplifications, the potential code could be used as a flight controller to be embedded in the MAV, allowing it to fly in an autonomous way.

[1] At the present time, the interface has been developed for one wing, in order to analyse the longitudinal flight of a MAV (more details in [15]).

Chapter 3

Modelling and Methodology

This chapter aims to explain the modelling of the unsteady potential model that computes the aerodynamic forces of a pair of flapping wings. To do that, both the wings and the wake left by them are modelled by discretising them into panels. Attached to each panel, there is a vortex ring that simulates the circulation of the wing and the vorticity of the wake.

In order to be able to develop a numerical model, it is necessary to start with a physical model. In this regard, the physical model is simplified to a mathematical model, from which the numerical model is derived.

Therefore, this chapter is divided into several sections, each of them focused on one model. To start with, the physical model of a flapping wing insect is discussed. Secondly, the physical model is mathematically expressed in terms of its kinematics and the equations that describe the aerodynamic flow around them. Lastly, it is explained how the mathematical expressions are discretised to build the numerical model. For this last section, the algorithm given in [16] is taken as starting point.

3.1 Physical Model

A flapping wing natural flyer or a vehicle must generate lift to counteract its weight and produce thrust to move forward. In order to produce the correct combination of forces for the current flight condition, natural flyers do not only flap their wings in a given way, but they also combine it with wing deformation, body contour, and tail movements [1], yielding a high complex motion. These motions are complex from the mechanical point of view, in terms of energy and power requirements; but also in terms of control and stability, particularly for the design of MAV

flight controllers. For this reason, the present document is concerned with the aerodynamic analysis only.

Following this approach, from an aerodynamic point of view, a flapping wing insect or vehicle has 2 well differentiated parts: the lifting surfaces and the body. Lifting surfaces are usually the wings and the stabilisers (e.g.: the tail). In flapping motion, wings are the producers of thrust and lift; whereas the stabilisers, if any, are in charge of stabilising the system, rather than producing lift or thrust. Hence, as the main purpose of this project is the computation of the aerodynamic forces, stabilising surfaces are no longer discussed in the following sections.

On the other hand, the body has two aerodynamic effects. First of all, it produces lift and drag. However, its contribution to the total forces can be neglected in comparison to that of the wings. Secondly, it interacts with the surrounding flow. Therefore, it modifies the flow pattern the wing would see without the body. The assessment of body-flow interaction requires the modelling of the body in the numerical aerodynamic model, thus increasing complexity and computational time. Since the effect is small, and the aim of the present project is developing a *low computational cost* model, the body is not modelled in this project.

In view of the above, it is necessary to model aerodynamic flow around the wings. To that end, it is necessary to be able to define the kinematics of the wings and derive a mathematical model for the flow. Following this line of thought, both issues are discussed in the following sections.

3.2 Kinematics of flapping motion

As it will be next in future sections, the instantaneous position and velocity of every point of the wing are necessary to be able to compute the aerodynamic model at every time instant.

3.2.1 Reference Frames

To define both position and velocity of the wing, several reference frames have to be set. In the most general approach, 4 different reference frames are required: an inertial or absolute reference frame which position and orientation are fixed; a reference frame attached to the body; and 2 moving references frames attached to each wing. The inertial reference frame is necessary in order to determine the absolute position and velocity of the wings. On the other hand, a reference frame attached to the wing is useful to formulate the aerodynamic equations, as it will be seen in § 3.3.3.

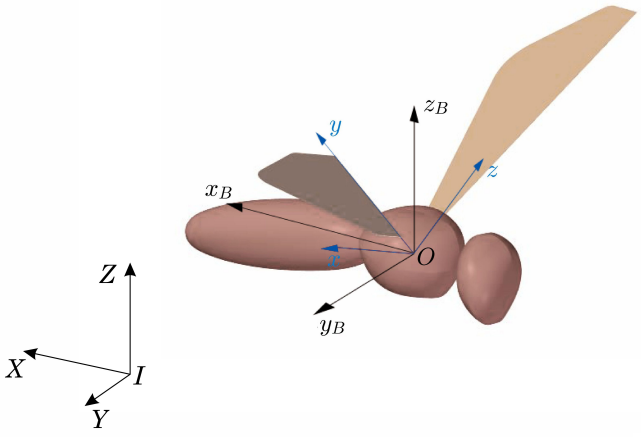

Figure 3.1: Insect model

Let the inertial reference frame be formed by 3 orthogonal axis, X,Y and Z, and be fixed at the inertial point I, so that the coordinate system is $IXYZ$. This reference frame is referred to as Σ_I. Likewise, the body fixed reference frame, Σ_B, is formed by the coordinate system $Ox_By_Bz_B$, as shown in Figure 3.1. The wing reference system, Σ_w, it is formed by the orthogonal system $Oxyz$ and is attached to the wing, moving with it. In Figure 3.1, only the reference frame of the right wing system is shown. When it is necessary to distinguish between right and left wing, subscript R and L will be used, respectively.

3.2.2 Position and Velocity

To maintain consistency throughout this paper, a specific notation will be followed to denote all position and velocity vectors that are used for the mathematical model. Vectors will appear in the equations in boldface.

The point a vector is referred to is the subscript of the vector; and the reference frame where the vector is expressed in, is its superscript. In this fashion, the position of point p, expressed in the inertial reference frame is $\boldsymbol{x}_p^I$. In this frame, it is assumed that the position is given with respect to the inertial point I. When position is given with respect to the origin of the body, O, it is called *relative position*, and it will be denoted with a prime, e.g.: $\boldsymbol{x}_p'^I$ is the relative position of point p with respect to O, expressed in Σ_I.

From the discussion above, the position of the body with respect to Σ_I is:

$$\boldsymbol{x}_O^I = (X_0, Y_0, Z_0) \tag{3.1}$$

And the absolute velocity of O is computed from eq. (3.1) as:

$$\boldsymbol{v}_O^I = \frac{d\boldsymbol{x}_O^I}{dt} = (\dot{X}_0, \dot{Y}_0, \dot{Z}_0) \tag{3.2}$$

Absolute position of a point p on the wing –i.e.: the position wrt[1] I– is obtained from the vector relationship:

$$\boldsymbol{x}_p = \boldsymbol{x}_O + \boldsymbol{x}'_p \tag{3.3}$$

From eq. (3.3), the absolute velocity of point p can be computed as:

$$\boldsymbol{v}_p = \frac{d\boldsymbol{x}_p}{dt} = \boldsymbol{v}_O + \boldsymbol{v}'_p + \boldsymbol{\Omega} \times \boldsymbol{x}'_p \tag{3.4}$$

In eq. (3.4), $\boldsymbol{\Omega}$ is the angular velocity of Σ_w wrt Σ_I; and $\boldsymbol{v}'_p$ is the relative velocity of p with respect to Σ_w. If the wing is assumed to be rigid, $\boldsymbol{v}'_p = 0$. Notice that eqs. (3.3) and (3.4) can be given in any reference frame, and therefore, no superscript is added.

It must be noted that eq. (3.4) has been obtained assuming that the body does not rotate wrt Σ_I. Nonetheless, the same equation can be applied if both Σ_B and Σ_w have an angular velocity. To do that, $\boldsymbol{\Omega}$ in eq. (3.4) is now the addition of both angular velocities.

3.2.3 Euler angles

Up to now, it has been stated that vectors can be expressed independently in any reference frame. However, it has not been explained yet how to change between reference frames. In this fashion, Euler angles will be used.

The definition of Euler angles allows not only to relate orientation between reference frames, but also to set the kinematics of the wings with respect to the body. To that end, 3 angles are selected:

- φ: is the flapping angle
- θ: is the pitch angle
- ψ: is the sweep angle

The physical meaning of these angles is depicted in Figure 3.2. There, the relationship between Σ_B and Σ_w is sketched. Nevertheless, the same picture could be applied if the body also rotates.

[1] *wrt* stands for *with respect to.*

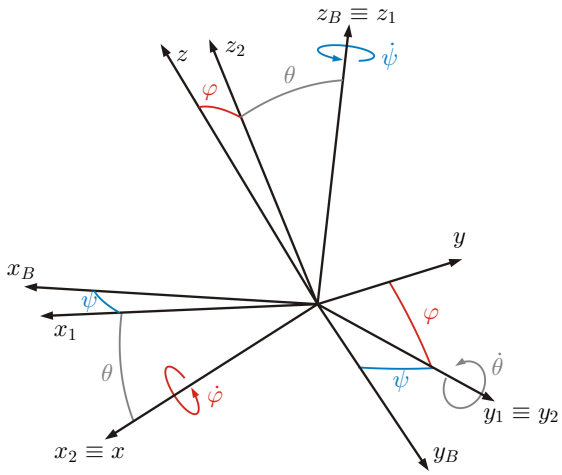

Figure 3.2: Eulerian rotation

From Figure 3.2, the meaning of the angles can be extracted. By imposing ψ and φ equal to 0, it is appreciated that θ is the instantaneous angle of attack of the wing. Similarly, by setting ψ and θ equal to zero, φ specifies the flap angle the of wing. Hence, a desired flapping motion is achieved by combination of time dependent functions of the 3 angles –i.e.: $\varphi = \varphi(t)$, $\theta = \theta(t)$ and $\psi = \psi(t)$–, as it is explained in § 3.2.4.

In order to express a vector in a different reference frame than the one it is expressed in, the so-called rotation matrices are used:

$$R_\phi = \begin{bmatrix} 1 & 0 & 0 \\ 0 & \cos\varphi & \sin\varphi \\ 0 & -\sin\varphi & \cos\varphi \end{bmatrix} \tag{3.5}$$

$$R_\theta = \begin{bmatrix} \cos\theta & 0 & -\sin\theta \\ 0 & 1 & 0 \\ \sin\theta & 0 & \cos\theta \end{bmatrix} \tag{3.6}$$

$$R_\psi = \begin{bmatrix} \cos\psi & \sin\psi & 0 \\ -\sin\psi & \cos\psi & 0 \\ 0 & 0 & 1 \end{bmatrix} \tag{3.7}$$

Therefore, given a vector $\boldsymbol{x}^B$, it can be expressed in Σ_w according to:

$$\begin{aligned} \boldsymbol{x}^{B_1} &= R_\psi \boldsymbol{x}^B \\ \boldsymbol{x}^{B_2} &= R_\theta \boldsymbol{x}^{B_1} \\ \boldsymbol{x}^w &= R_\varphi \boldsymbol{x}^{B_2} \end{aligned}$$

Thus:

$$\boldsymbol{x}^w = R_\varphi R_\theta R_\psi \boldsymbol{x}^B \tag{3.8}$$

Rotation matrices from eqs. (3.5), (3.6) and (3.7) are orthonormal matrices. Hence, the inverse relationship of (3.8) can be written as:

$$\boldsymbol{x}^B = R_\psi^T R_\theta^T R_\varphi^T \boldsymbol{x}^w \tag{3.9}$$

It should be highlighted that the previous development is applicable to any vector, such as linear and angular velocity, not only position.

3.2.4 Kinematic Equations

Now that all aspects related to coordinate systems and vector operations are derived, it is possible to appropriately set sytems's kinematics. If the body were modelled, it would be necessary to know the specific orientation of Σ_B. However, from discussion of § 3.1, it was concluded only the aerodynamics of the wings are modelled. Therefore, only the kinematics of the wings have to be set. Following this line of thought, it is assumed that the axes of Σ_B are aligned to those of Σ_I.

In § 3.2.2, it was explained how to compute the linear velocity of O knowing the position as a function of time, namely $\boldsymbol{x}_O^I(t)$. However, it is more usual to prescribe the velocity and compute the position, $\boldsymbol{x}_O^I$, from integration. In this fashion, the velocity of point O is prescribed according to:

$$\boldsymbol{v}_O^I(t) = (\dot{X}_O(t), \dot{Y}_O(t), \dot{Z}_O(t)), \tag{3.10}$$

being $\dot{X}_O(t)$, $\dot{Y}_O(t)$, and $\dot{Z}_O(t)$ known functions of time.

Orientation and angular velocity of Σ_w are obtained following a similar approach. Euler angles are prescribed to be functions of time, that is:

$$\begin{aligned} \varphi &= \varphi(t) \\ \theta &= \theta(t) \\ \psi &= \psi(t) \end{aligned} \tag{3.11}$$

Previous functions are typically periodic functions. The angular velocity can be computed from derivation. Therefore:

$$\boldsymbol{\Omega} = \dot{\psi}\boldsymbol{k}_B + \dot{\theta}\boldsymbol{j}_2 + \dot{\varphi}\boldsymbol{i}_w, \tag{3.12}$$

where $\boldsymbol{i}$, $\boldsymbol{j}$ and $\boldsymbol{k}$ are unitary vectors in x, y and z directions.

For the development of the aerodynamic model, angular velocity in eq. (3.12) has to be expressed in Σ_w. Using rotation matrices of eqs. from (3.5) to (3.7) it is possible to show that:

$$\boldsymbol{\Omega} = p\,\boldsymbol{i}_w + q\,\boldsymbol{j}_w + r\,\boldsymbol{k}_w, \tag{3.13}$$

being:

$$\begin{aligned} p &= \dot{\varphi} - \dot{\psi}\sin\theta, \\ q &= \dot{\theta}\cos\varphi - \dot{\psi}\cos\theta\sin\varphi, \\ r &= -\dot{\theta}\sin\varphi + \dot{\psi}\cos\theta\cos\varphi. \end{aligned} \tag{3.14}$$

Hence, by prescribing (3.10) and (3.11), wings' kinematics are completely defined. Notice that the development has been undertaken for one wing, but the same applies for the other wing. When both wings are considered, $\boldsymbol{v}_0$ is the same, but the expressions of eq. (3.11) can be set to represent a symmetric motion or an asymmetric one. The setting down of the kinematics is clearly understood with the examples of Chapters 4 and 5.

3.3 Aerodynamic Model

Once the kinematics of flapping wing motion has been defined, it is now time to describe the fundamental equations that define aerodynamic flow around the wings. Therefore, this section is aimed to derive the mathematical expressions that are needed to compute aerodynamic forces on the wings. To that end, Navier-Stokes equations, that define the motion of a fluid, are set down. After that, they are simplified to derive Euler's eqs, which set the mathematical model that will be used as a basis of the low-order numerical model here presented.

3.3.1 Navier-Stokes equations

Navier-Stokes equations are the fundamental equations of Fluid Mechanics, relating local properties of a flow: velocity $\boldsymbol{v}(\boldsymbol{x}, t)$, density $\rho(\boldsymbol{x}, t)$, and entropy $s(\boldsymbol{x}, t)$.

Derivation of these equations is complex and is not relevant for the present project. Therefore, they are simply written down below, as extracted from [17].

$$\frac{\partial \rho}{\partial t} + \nabla \cdot (\rho \boldsymbol{v}) = 0 \tag{3.15}$$

$$\rho \frac{\partial \boldsymbol{v}}{\partial t} + \rho \boldsymbol{v} \nabla \cdot \boldsymbol{v} = -\nabla p + \nabla \cdot \bar{\bar{\tau}}' + \rho \boldsymbol{f}_m \tag{3.16}$$

$$\rho T \frac{Ds}{Dt} = \phi_v - \nabla \cdot \boldsymbol{q} + Q_c + Q_r \tag{3.17}$$

The previous equations are conservation equations of continuity, momentum, and entropy, respectively. The following notation has been employed: p is pressure; $\bar{\bar{\tau}}'$ is the viscous stress tensor; $\boldsymbol{f}_m$ are the mass forces; T is the fluid temperature; ϕ_v is the deformation work due to viscous dissipation ($\phi_v = \bar{\bar{\tau}}' : \nabla \boldsymbol{v}$); $\boldsymbol{q}$ is the heat rate; and Q_c and Q_r are the rates of heat release due to chemical reaction and radiation. Notice that the previous quantities are local properties of the fluid, therefore, they are function of position and time, i.e.: $f(\boldsymbol{x}, t)$.

Eqs. from (3.15) to (3.17) describe all fluid motions. To that purpose, Navier-Stokes equations must be complemented with boundary conditions on the boundaries of the flow field [17]. For flows around solid bodies, as it the case, boundary conditions are specified in terms of velocity at the body surface; thus, it is set to be equal to the velocity of the body surface at that point. This condition is known as *non-slip condition*. Furthermore, when flow motion is unsteady, Navier-Stokes equations also require initial conditions of the fluid.

Typically, Navier-Stokes equations are simplified to be solved. In the following subsection, simplifications are carried out to develop the low-order model that is implemented in this project.

3.3.2 Unsteady Euler equations

To build the numerical model, a simplified version of Navier-Stokes equations is considered. First of all, it is assumed that air is a perfect gas and a simple substance. Therefore, the local value of any thermodynamic variable can be defined by any other two independent thermodynamic variables [17]. For instance, local pressure at a point and at a given instance can be written as $p = p(s, \rho)$.

For gases such as air, mass forces have a negligible effect in fluid motion compared to the convective acceleration of the fluid, that is:

$$Fr = \frac{\mathcal{O}(\rho \boldsymbol{v} \cdot \nabla \boldsymbol{v})}{\mathcal{O}(\rho \boldsymbol{f_m})} \gg 1,$$

being Fr the Froude number. Therefore, the last term in eq. (3.16) is negligible and can be neglected. The Reynolds number, Re, was already defined in § 1. From a physical point of view, it is the ratio between convective and viscous effects, yielding:

$$R_e \sim \frac{\rho \boldsymbol{v} \nabla \boldsymbol{v}}{\mu \nabla^2 \boldsymbol{v}} \sim \frac{\rho U_c l_c}{\mu} \tag{3.18}$$

Typically, $Re \gg 1$, and viscous effects can be neglected. This is not true near the body surface, where velocity is 0. However, for streamlined shaped bodies, the region where viscous effects are important are confined in a thin region, namely the boundary layer, which remains attached to the body; therefore, the hypothesis stating that viscous effects are negligible holds in all the flow field except inside the boundary layer [16]. Nonetheless, due to flapping motion characteristics and different flight conditions, such as hovering flight, boundary layer separation is prone to occur and viscosity effects become important. Despite that, for the sake of simplicity, it is assumed $Re \gg 1$ and viscous effects are neglected in eqs. (3.16) and (3.17).

In the case of air, Prandtl number[2] is $Pr = 0.7$. For $Re \gg 1$ and $Pr \sim 1$, it can be shown (see [17]) that thermal heat conduction ($\nabla \cdot \boldsymbol{q}$ in eq. (3.17)) can be neglected. From the previous assumptions, and neglecting radiation and chemical reactions, i.e.: $Q_c = Q_r = 0$, Navier-Stokes equations take the form of the so-called Euler equations:

$$\frac{\partial \rho}{\partial t} + \nabla \cdot (\rho \boldsymbol{v}) = 0 \tag{3.19}$$

$$\rho \frac{\partial \boldsymbol{v}}{\partial t} + \rho \boldsymbol{v} \nabla \cdot \boldsymbol{v} = -\nabla p \tag{3.20}$$

$$\frac{Ds}{Dt} = 0 \tag{3.21}$$

Notice that from eq. (3.21) the entropy of each fluid particle remains constant; thus, if entropy far from the body is constant and equal to s_0, $s = s(t = 0) = s_0$, and flow is isentropic. This entails that pressure can be expressed as a function of density only, since:

$$p = p(s_0, \rho) = p(\rho) \tag{3.22}$$

3.3.3 Potential Flow

In this section, it will be proven that aerodynamic flow that is being analysed can be treated as a potential flow. In this way, it will be possible to solve the resulting

[2] $Pr = \nu/\alpha$, is the ratio of molecular transport rates of momentum and heat. Being ν the kinematic viscosity and α the thermal diffusivity

equations, using the so-called Green's identity. To that end, we must first define what a potential flow is.

When a flow is potential, the velocity field can be described by a scalar function, $\phi(\boldsymbol{x}, t)$, such that:

$$\boldsymbol{v}(\boldsymbol{x}, t) = \nabla\phi(\boldsymbol{x}, t), \tag{3.23}$$

where $\phi(\boldsymbol{x}, t)$ is called *velocity potential*. Recalling that the curl of a gradient is always 0, i.e.: $\nabla \times (\nabla f) = 0$, (being f a scalar function); and that vorticity is defined as:

$$\boldsymbol{\omega} = \nabla \times \boldsymbol{v} \tag{3.24}$$

It follows that:

$$\boldsymbol{\omega} = \nabla \times (\nabla\phi) = 0 \tag{3.25}$$

Thus, from eq. (3.25) one can state that flow is irrotational. Based on this result, it will be demonstrated throughout the following discussion, that the present flow is irrotational; and therefore, the velocity field can be expressed in terms of a *velocity potential*.

Before carrying on, another simplification is undertaken. Typical speed of animals and MAV are low as compared to sound speed; thus, compressibility effects can be neglected and ρ of can be assumed constant [18]. Therefore, for the envisaged application, the previous equations can be rewritten as:

$$\nabla \cdot \boldsymbol{v} = 0 \tag{3.26}$$

$$\frac{\partial \boldsymbol{v}}{\partial t} + \nabla\frac{\|\boldsymbol{v}\|^2}{2} - \boldsymbol{v} \times (\nabla \times \boldsymbol{v}) = -\frac{1}{\rho}\nabla p \tag{3.27}$$

Notice that the second term of eq. (3.20) has been rewritten in eq. (3.27) in a more suitable form for the following discussion. Now, taking the curl in eq. (3.27),

$$\frac{\partial \boldsymbol{\omega}}{\partial t} - \nabla \times (\boldsymbol{v} \times \boldsymbol{\omega}) = 0. \tag{3.28}$$

From the algebraic relationship (see [19]):

$$\nabla \times (\boldsymbol{v} \times \boldsymbol{\omega}) = \boldsymbol{v}\nabla \cdot \boldsymbol{\omega} - \boldsymbol{\omega}\nabla \cdot \boldsymbol{v} + \boldsymbol{\omega} \cdot \nabla\boldsymbol{v} - \boldsymbol{v} \cdot \nabla\boldsymbol{\omega}, \tag{3.29}$$

and making use of eq. (3.26) and the fact that $\nabla \cdot (\nabla \times \boldsymbol{f}) = 0$; the first two terms of (3.29) vanish. Therefore, eq. (3.28) takes the form:

$$\frac{\partial \boldsymbol{\omega}}{\partial t} + \boldsymbol{v} \cdot \nabla\boldsymbol{\omega} = \boldsymbol{\omega} \cdot \nabla\boldsymbol{v} \tag{3.30}$$

The left hand side of eq. (3.30) is the material derivative of the vorticity. Hence:

$$\frac{D\boldsymbol{\omega}}{Dt} = \boldsymbol{\omega} \cdot \nabla \boldsymbol{v} \tag{3.31}$$

Eq. (3.31) is the simplified version of the so-called *Helmholtz vorticity transport equation* when flow is isentropic and incompressible. Therefore, it is seen that under the previous assumptions, the variation of vorticity following a given particle is only due to term $\boldsymbol{\omega} \cdot \nabla \boldsymbol{v}$, which represents the *vortex stretching* and *vortex tilting*. However, it is shown in the next paragraphs that no generation of vorticity is produced in the problem of interest.

An insect or MAV in forward flight, moving with a velocity $-U_\infty \boldsymbol{i}$, can be seen as a body immersed in a fluid with free stream a U_∞. Under these conditions, the vorticity at the free stream is 0, since $\boldsymbol{\omega} = \nabla \times U_\infty \boldsymbol{i} = 0$ (see Figure 3.3).

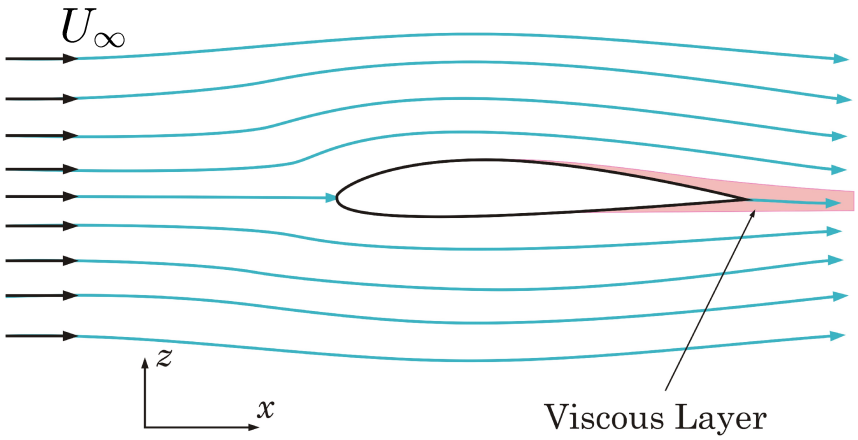

Figure 3.3: Three dimensional body immersed in a free stream

Therefore, from integration of eq. (3.31) with initial condition $\boldsymbol{\omega} = 0$, it is obtained that the variation of vorticity of a fluid particle is 0 at any given instant of time, [17].

As a conclusion to the previous discussion, it is seen that flow is irrotational, with the execption of a thin layer attached to the body and at the wake, where viscous effects are important and vorticity is generated. In this fashion, the velocity field can be expressed as a function of the *velocity potential*, as given in eq. (3.23).

Inserting eq. (3.23) into eqs. (3.26) and (3.27) the following equations are obtained:

$$\nabla^2\phi = 0 \tag{3.32}$$

$$\rho\frac{\partial\phi}{\partial t} + \rho\frac{\|\nabla\phi\|^2}{2} + p = C(t) \tag{3.33}$$

Eq. (3.33) is the so-called *Unsteady Bernoulli's equation*. The integration constant, $C(t)$ can be evaluated at a point where pressure and velocity potential are known. Particularly, for the problem of a body moving in an otherwise undisturbed flow –like the case of a flapping wing MAV in the air–, C can be evaluated at infinity, where $p = p_\infty$ and the fluid is at rest. Under these conditions $C = p_\infty$ in eq. (3.33).

Boundary Conditions

Eq. (3.32) is the well-Known Laplace equation. In order to solve it, two boundary conditions are required. It was stated in § 3.3.1 that for a body moving inside a fluid, the required boundary condition is the so-called *non-slip boundary condition*. However, by neglecting viscous effects of eq. (3.16), it is not possible to fulfil it. Instead, in inviscid flow, the *impermeability boundary condition* is set. That means velocity normal to the body's surface at the surface is set to zero, but a tangential velocity is allowed.

For the present problem, if the surface of the wing is defined as:

$$z(x, y) = \eta(x, y), \tag{3.34}$$

it is possible to find a function such that:

$$F_S(x, y, z) \equiv z - \eta(x, y) = 0. \tag{3.35}$$

Therefore, the vector normal to the wing's surface is:

$$\boldsymbol{n} = \frac{\nabla F_S}{|\nabla F_S|} \tag{3.36}$$

(Notice that previous expressions hold for any reference frame). When imposing zero normal flow across the surface, one must recall that the wing has its own kinematics. Taking into account that $\nabla\phi$ is the fluid velocity seen from the inertial

reference frame, Σ_I, the local fluid velocity at a point p seen in the wing reference frame, Σ_w, is computed according to:

$$\boldsymbol{v}_{rel}(\boldsymbol{x}_p, t) = \nabla\phi - \boldsymbol{V}_p \tag{3.37}$$

Being $\boldsymbol{V}_p$ the absolute kinematic velocity of point p as computed from eq. (3.4):

$$\boldsymbol{V}_p = \boldsymbol{v}_O + \boldsymbol{v}'_p + \boldsymbol{\Omega} \times \boldsymbol{x}'_p$$

Capital $\boldsymbol{V}$ is used from now on to denote velocity of a point whenever it refers to eq. (3.4). This is done in order to avoid confusion between velocity of a solid point belonging to the wings and velocity of the fluid.

It should be noted that $\boldsymbol{v}'_p \neq \boldsymbol{v}_{rel}$. Whereas $\boldsymbol{v}'_p$ is the relative velocity of point p with respect to Σ_w, $\boldsymbol{v}_{rel}$ is the fluid velocity at point p seen from Σ_w. For a rigid wing –or without movable parts, such as flaps–, $\boldsymbol{v}'_p = 0$. In Figure 3.4 the previous magnitudes are sketched.

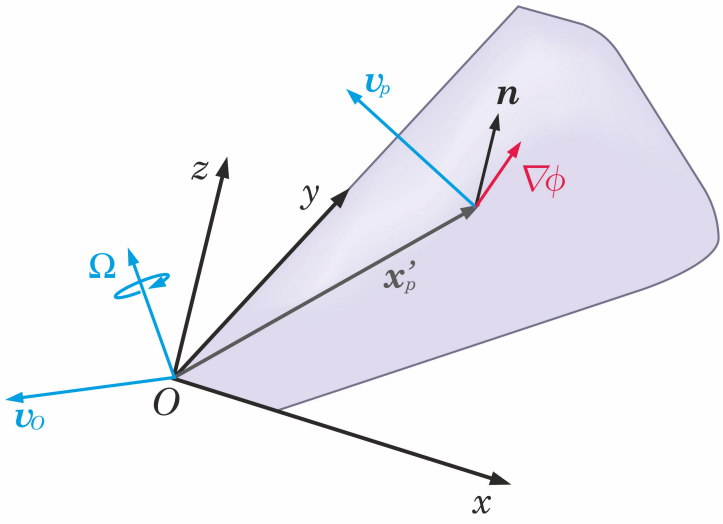

Figure 3.4: Velocity of a point p

Finally, zero normal flow is imposed according to:

$$\boldsymbol{v}_{rel} \cdot \boldsymbol{n} = 0 \tag{3.38}$$

Hence, combining eqs. (3.37) and (3.38),

$$\nabla\phi \cdot \boldsymbol{n} = \boldsymbol{V}_p \cdot \boldsymbol{n}. \tag{3.39}$$

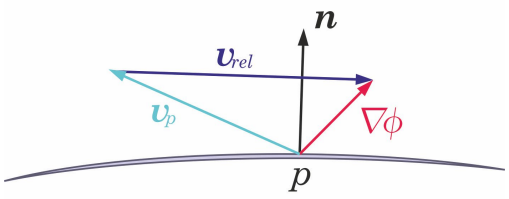

Figure 3.5: Zero normal flow across the surface boundary condition

In Figure 3.5 this condition is displayed.

The second boundary condition is the *freestream boundary condition*. Far away from the body, the potential has to have the value at such point. Since air remains undisturbed far away from the body,

$$\lim_{\boldsymbol{x}\to\infty} \boldsymbol{v} = 0$$

Therefore, the *velocity potential*, ϕ, at $\boldsymbol{x} \to \infty$ is a constant value that can be set, without lost of generality, equal to 0. Thus:

$$\lim_{\boldsymbol{x}\to\infty} \phi = 0 \tag{3.40}$$

From the previous condition, it is inferred that ϕ has the effect of disturbing the flow in the vicinity of the wing that otherwise remains steady; for that reason, it is often denoted as *perturbation potential*.

Method of solution: Green's identity

Once boundary conditions have been deduced, the *velocity potential* has to be calculated to satisfy eq. (3.32). In order to do that, *Green's Identity* is used. Following this approach, the *velocity potential* at a point P of the fluid yields to be (see Chapter 3 of [16] for a complete derivation):

$$\phi(\boldsymbol{x}_P) = \frac{1}{4\pi}\int_{S_w}\left[\frac{\partial\phi}{\partial n}\left(\frac{1}{r}\right) - \phi\frac{\partial}{\partial n}\left(\frac{1}{r}\right)\right]dS - \frac{1}{4\pi}\int_{S_k}\phi\frac{\partial}{\partial n}\left(\frac{1}{r}\right)dS \tag{3.41}$$

Integration surfaces in eq. (3.41) are sketched in Figure 3.6. Likewise, it must be noticed that the normal vector, $\boldsymbol{n}$, points outwards for the integration volume V.

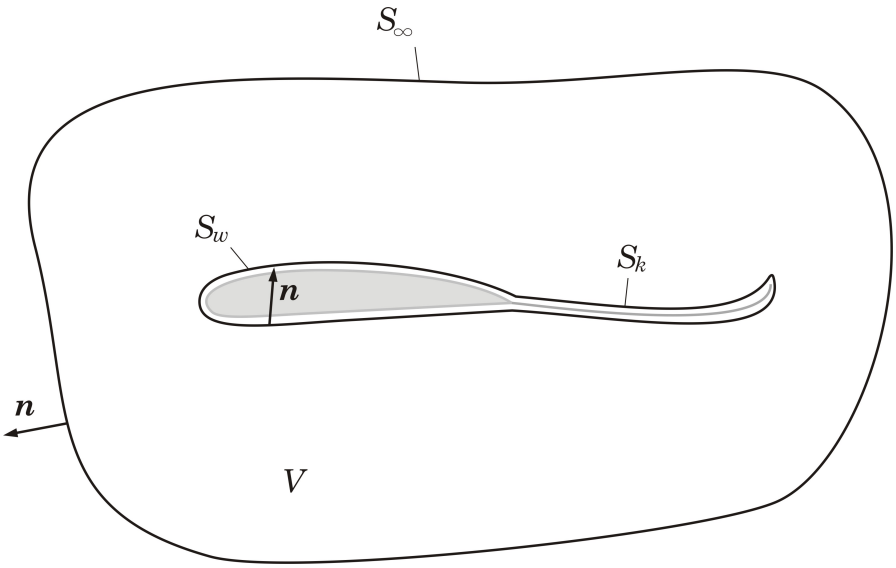

Figure 3.6: Potential problem for a lifting body

In this fashion, term $\partial/\partial n$ is equal to $\nabla(\quad)\cdot\boldsymbol{n}$; being $\boldsymbol{n}$ the normal vector to the surface in the direction previously stated.

S_w is the surface of the wing, and S_k is the surface of the wake. The existence of a layer where vorticity is confined was already commented in § 3.3.3. This boundary surface has to be included since there is a discontinuity in the *velocity potential* across it. This can be proven through *Kelvin's Circulation theorem* (see Ref. [19]).

The strength of eq. (3.41) lies in its capability of expressing the value of ϕ at any point inside region V just by knowing the value of the potential at wing's and wake's surfaces. Furthermore, terms inside the integrals can be rewritten as:

$$\sigma = -\frac{\partial\phi}{\partial n} \qquad\qquad \mu = -\phi \tag{3.42}$$

Consequently, eq. (3.41) is rewritten as:

$$\phi(\boldsymbol{x}_P) = -\frac{1}{4\pi}\int_{S_w}\left[\sigma\left(\frac{1}{r}\right) - \mu\frac{\partial}{\partial n}\left(\frac{1}{r}\right)\right]dS + \frac{1}{4\pi}\int_{S_k}\mu\frac{\partial}{\partial n}\left(\frac{1}{r}\right)dS \tag{3.43}$$

In eq. (3.43), σ and μ are called *source* and *doublet*. They are elementary solutions to the potential flow (see [16] for more details). Therefore, the problem of computing ϕ at any fluid point P in region V reduces to find the source strength distribution along wing's surface and the doublet strength distribution along wing and wake's surfaces. Likewise, one can appreciate that by using these elementary

solutions, both terms of eq. (3.41) decay as $\boldsymbol{x}_P \to \infty$, i.e.: $\phi(\infty) = 0$; thus, boundary condition of eq. (3.40) is automatically satisfied.

Having reached this point, another simplification is introduced, i.e.: it is assumed that the wings are infinitely thin. Therefore, if we choose a coordinate system whose x and y directions are tangent to the surface, the normal vector on the upper and lower surface at a given point are related through:

$$\boldsymbol{n}(0^+) = -\boldsymbol{n}(0^-) \tag{3.44}$$

Similarly, from Figure 3.7:

$$\left.\frac{\partial\phi}{\partial n}\right|_{z=0^+} = -\left.\frac{\partial\phi}{\partial z}\right|_{z=0^+} \tag{3.45}$$

$$\left.\frac{\partial\phi}{\partial n}\right|_{z=0^-} = \left.\frac{\partial\phi}{\partial z}\right|_{z=0^-} \tag{3.46}$$

In the same fashion, since the wing is infinitely thin, kinematic velocity at a given point of the wing is (using the reference frame of Figure 3.7):

$$\boldsymbol{v}_p(x, y, 0^+) = \boldsymbol{v}_p(x, y, 0^-)$$

Therefore, using eq. (3.44),

$$\boldsymbol{v}_p(0^+) \cdot \boldsymbol{n}(0^+) = -\boldsymbol{v}_p(0^-) \cdot \boldsymbol{n}(0^-) \tag{3.47}$$

Finally, combining eqs. (3.47), (3.45) and (3.45) and making use of eq. (3.39), it is straightforward to show that:

$$\left.\frac{\partial\phi}{\partial z}\right|_{z=0^+} = \left.\frac{\partial\phi}{\partial z}\right|_{z=0^-} \tag{3.48}$$

Hence, the source distribution along the wing vanishes, since:

$$\frac{1}{4\pi}\int_{S_w} \frac{\partial\phi}{\partial n}\left(\frac{1}{r}\right) dS = \frac{1}{4\pi}\int_{S_w} \frac{1}{r}\left[\left.\frac{\partial\phi}{\partial z}\right|_{z=0^-} - \left.\frac{\partial\phi}{\partial z}\right|_{z=0^+}\right] dS = 0 \tag{3.49}$$

Finally, as it has been demonstrated, the present problem is reduced to finding the doublet strength distribution on the wing's and wake's surfaces, according to:

$$\phi(\boldsymbol{x}_P) = \frac{1}{4\pi}\int_{S_w} \mu\frac{\partial}{\partial n}\left(\frac{1}{r}\right) dS + \frac{1}{4\pi}\int_{S_k} \mu\frac{\partial}{\partial n}\left(\frac{1}{r}\right) dS, \tag{3.50}$$

what satisfies the boundary condition in eq. (3.39).

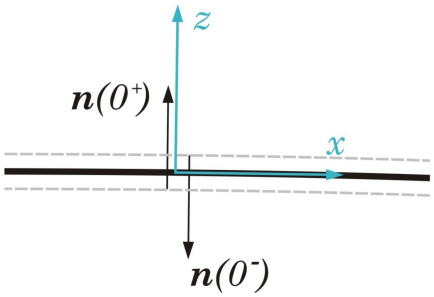

Figure 3.7: Infinite thin wing

Pressure Calculation

Equation (3.32), combined with eqs. (3.39) and (3.40), allows to compute the *potential velocity*. In turn, it is plugged in eq. (3.33) (which is written below) to obtain the pressure from which the aerodynamics forces are computed.

$$\rho\frac{\partial\phi}{\partial t}+\rho\frac{\|\nabla\phi\|^2}{2}+p=p_\infty \tag{3.51}$$

It must be noted that eq. (3.51) is expressed in the inertial reference frame. The spatial derivative $\nabla\phi$ is independent of the reference frame, but time derivatives have to be performed at a spatial point that is inertial.

By the formulation above to solve the potential flow problem, ϕ is computed at a point that is not inertial, $\boldsymbol{x}'_p$. However, in order to solve eq. (3.51), the time derivative must be expressed in an inertial reference frame $\boldsymbol{x}_p$. By denoting the time derivative in the moving reference frame as:

$$\dot{\phi}=\left.\frac{\partial\phi}{\partial t}\right|_w$$

Chain rule is applied to relate the inertial time derivative in eq. (3.51). Namely:

$$\dot{\phi}=\left.\frac{\partial\phi}{\partial t}\right|_I+\frac{\partial\phi}{\partial\boldsymbol{x}_p}\frac{\partial\boldsymbol{x}_p}{\partial t} \tag{3.52}$$

In eq. (3.52), first term is the time derivative as written in eq. (3.51). Left hand side of the second term is just a way of writing $\nabla\phi$; likewise, right hand side is $\boldsymbol{v}_p$,

as it is seen from eq. (3.4). Therefore:

$$\dot{\phi} = \left.\frac{\partial \phi}{\partial t}\right|_I + \nabla\phi\, \boldsymbol{v}_p \tag{3.53}$$

According to that, pressure at a given fluid point is computed according to:

$$p = p_\infty - \frac{1}{2}\rho\|\nabla\phi\|^2 + \rho\nabla\phi\, \boldsymbol{v} - \rho\dot{\phi} \tag{3.54}$$

This latter equation can be rearranged –by using eq. (3.39)–, to eq. (**??**)eq:pressure), which is more suitable form for future derivations.

$$p = p_\infty + \frac{1}{2}\rho\|\boldsymbol{v}\|^2 - \frac{1}{2}\rho\|\boldsymbol{v}_{rel}\|^2 - \rho\dot{\phi} \tag{3.55}$$

3.4 Numerical Model

In this section, the analytical equations derived above are discretised so they can be implemented numerically in a computing software. Particularly, the employed computing software is MATLAB®. The numerical method used is a panel method based on vortex ring elements. In a panel model, the wing and the wake are discretised into panels. Each panel in the wing has a constant circulation (or doublet strength) which is unknown, and a control point. In this fashion, the circulation of each panel is determined by imposing the *zero normal flow* at the control points and computing the circulation distribution of the panels that fulfils it by means of a system of linear algebraic equations.

In the present section, the geometry discretisation; the reduction of the analytical equations to a set of linear algebraic equations; the modelling of the wake; and the forces computations are presented. The derivation followed herein is based on Chapter 13 of [16]. In turn, the developed code is based on the one written in [16] for a wing that is suddenly accelerated. Therefore, the numerical model is firstly explained under the assumption that there is only one wing, and later, the modifications that have to be implemented when there are two wings present are discussed.

3.4.1 Wing and wake discretisation

The wing surface is divided into N panels (i_N chordwise panels and j_N spanwise panels). Thus, let us define the chordwise length of each panel as Δx_{ij} and the

spanwise length as Δy_{ij}. A *control point* is associated to each panel. This *control point* is placed in the middle of the spanwise panel length and at $3/4\Delta x_{ij}$. Similarly, the head of the vortex ring is placed at $1/4\Delta x_{ij}$ and its end is placed at $1/4\Delta x_{ij}$ of the next panel. Circulation, Γ_{ij} of each panel is unknown, and it is determined by imposing the boundary condition of eq. (3.39) at every *control point*.

Since the method is unsteady, the wake is being formed by vortex rings that are shed as the wing moves. The circulation of the wake panels is determined by those of the wing and is set to fulfil *Kelvin's Circulation theorem*, as explained in § 3.4.3. The previous descriptions are illustrated in Figure 3.8.

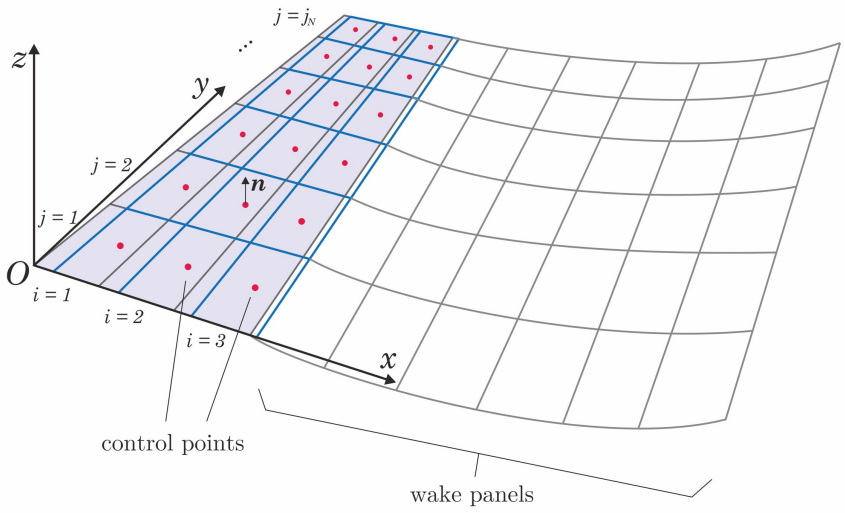

Figure 3.8: Wing and wake discretization

Vortex Ring

Before carrying on, a brief definition of a vortex ring must be provided. Nonetheless a more detailed explanation is provided in Appendix A. A vortex ring is a vortex filament which, in accordance to Helmhotz's theorems, is closed and has constant strength, Γ. According to *Biot-Savart law* the induced velocity on a fluid point by a vortex ring is:

$$\nabla\phi(\boldsymbol{x}_p) = \frac{\Gamma}{4\pi}\oint_C \frac{d\boldsymbol{l}\times\boldsymbol{r}}{r^3} \tag{3.56}$$

In eq. (3.56), Γ is the circulation: $d\boldsymbol{l}$ is the differential length of the vortex ring;

and $\boldsymbol{r}$ is the vector between the differential length of the vortex ring segment and the position of the fluid point, as illustrated in Figure 3.9.

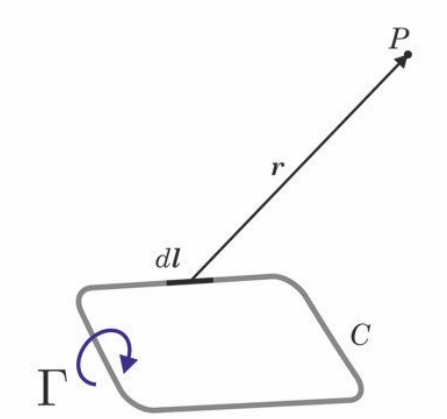

Figure 3.9: Vortex Ring

It must be noted that the usual approach is to take advantage of wing's symmetry with respect to the longitudinal axis, to model half of the wing, and apply symmetry to solve the problem. In this fashion, the computational cost is reduced. Similarly, when modelling 2 wings, it is also usual to model 1 wing. However, in this project it has been decided to model the complete geometry, with the aim of being able to study asymmetric flight conditions in the future (see Chapter 6).

3.4.2 Reduction of the problem to a set of Linear Algebraic Equations

As discussed in eq. (3.55), in order to compute the aerodynamic forces it is necessary to calculate the potential velocity, $\nabla\phi$. To that end, eq. (3.50) is plugged into eq. (3.39).

Once the wing has been divided into panels, it is possible to impose eq. (3.39) at each *control point* simultaneously to compute the circulation of each panel required to fulfil the boundary condition at the N *control points*. Having reached this point, it is noteworthy to mention that eq. (3.50) was expressed in terms of a doublet strength distribution instead of circulations. However, it can be proven that the velocity induced by a panel with constant doublet strength is equivalent to the one induced by a vortex ring provided that $\mu = \Gamma$, being the former the doublet strength of the panel (see Chapter 10.4 of [16]). Following this approach, the

normal induced velocity at a given point can be written as:

$$\nabla\phi \cdot \boldsymbol{n} = \left(\sum_{l=1}^{N_w} \frac{\Gamma_l}{4\pi} \oint_C \frac{d\boldsymbol{l} \times \boldsymbol{r}}{r^3} + \sum_{k=1}^{N_k} \frac{\Gamma_k}{4\pi} \oint_C \frac{d\boldsymbol{l} \times \boldsymbol{r}}{r^3} \right) \cdot \boldsymbol{n}, \tag{3.57}$$

where the first term corresponds to induced velocity by the N panels of the wing, and the second term corresponds to the induced velocity by the wake panels. Now, plugging eq. (3.57) into eq. (3.39), yields:

$$\sum_{l=1}^{N_w} \frac{\Gamma_l}{4\pi} \oint_C \frac{d\boldsymbol{l} \times \boldsymbol{r}}{r^3} \cdot \boldsymbol{n} + \nabla\phi_k \cdot \boldsymbol{n} = \boldsymbol{V}_p \cdot \boldsymbol{n}, \tag{3.58}$$

where the induced velocity on the control point by all the wake panels has been denoted as $\nabla\phi_k$.

In eq. (3.58), the point velocity, $\boldsymbol{V}_p$ is known. Likewise, as it will be seen in § 3.4.3, the circulation of the wake panels –i.e.: Γ_k– is known; hence, the induced velocity by the wake can be calculated. Furthermore, for a single wing panel, the induced velocity depends on the panel's geometry. Therefore, the only unknowns are the circulations of the wing's panels, Γ_l. As a consequence, there are N unknowns and N control points where eq. (3.58) can be imposed. This yields a system of N equations with N unknonwns that can be solved. To that end, the first term of eq. (3.58) can be rewritten:

$$\frac{1}{4\pi} \oint_C \frac{d\boldsymbol{l} \times \boldsymbol{r}}{r^3} \cdot \boldsymbol{n} \Big|_l \equiv a_l, \tag{3.59}$$

where the subscript l refers to a given panel. a_l is known as *influence coefficient*, since it represents the velocity the panel would induce with a unitary circulation. Therefore, for a given control point, eq. (3.58) is rewritten as:

$$\sum_{l=1}^{N_w} a_l \Gamma_l + \nabla\phi_k \cdot \boldsymbol{n} = \boldsymbol{V}_p \cdot \boldsymbol{n} \tag{3.60}$$

If the same equation is written for the N *control points*, the resulting system of equations,

$$\begin{aligned}
a_{11}\Gamma_1 + a_{12}\Gamma_2 + ... + a_{1N}\Gamma_N &= v_{n_1} - \nabla\phi_k|_1 \cdot \boldsymbol{n}_1 \\
a_{21}\Gamma_1 + a_{22}\Gamma_2 + ... + a_{2N}\Gamma_N &= v_{n_2} - \nabla\phi_k|_2 \cdot \boldsymbol{n}_2 \\
&\vdots \\
a_{N1}\Gamma_1 + a_{N2}\Gamma_2 + ... + a_{NN}\Gamma_N &= v_{n_N} - \nabla\phi_k|_N \cdot \boldsymbol{n}_N
\end{aligned}$$

can be rewritten in matrix form, yielding:

$$\begin{pmatrix} a_{11} & a_{12} & \cdots & a_{1N} \\ a_{21} & a_{22} & \cdots & a_{2N} \\ \vdots & \vdots & \ddots & \vdots \\ a_{N1} & a_{N2} & \cdots & a_{NN} \end{pmatrix} \begin{pmatrix} \Gamma_1 \\ \Gamma_2 \\ \vdots \\ \Gamma_N \end{pmatrix} = \begin{pmatrix} RHS_1 \\ RHS_2 \\ \vdots \\ RHS_N, \end{pmatrix} \tag{3.61}$$

where RHS_l stands for *right hand side* of the equation, namely,

$$RHS_l = v_{n_l} - \nabla\phi_k|_l \cdot \boldsymbol{n}_l,$$

being v_{n_l} the normal velocity, and $\nabla\phi_k|_l$ the induced velocity at the control point l. The subscripts of the *influence coefficients*, a_{kl}, correspond to the control point and the panel that induced the velocity, respectively. In this fashion, a_{kl} is the normal velocity at the control point k induced by the vortex ring of panel l if it had $\Gamma_l = 1$.

Since the problem is unsteady, the right hand side of the matrix equation in eq. (3.61) changes with time. Therefore, eq. (3.61) has to be solved through time. To that end, time is disretised into time steps, such that the momentary time is written as:

$$t = i_t \Delta t$$

where i_t is the time step counter, and Δt is step size or time length. The latter is defined as the characteristic time a fluid particle needs to travel 1/4 of a panel. Thus:

$$\Delta t = \frac{c/i_N}{4U_c}, \tag{3.62}$$

being c the chord of the wing and U_c a characteristic velocity.

The main advantage of this formulation is that this matrix equation is easily solved using MATLAB. Furthermore, since the boundary condition is expressed in the wing reference frame, Σ_w, the *influence coefficients*, a_{kl} are computed only once, since the geometry of the wing remains constant with time.

3.4.3 Physical considerations for the wake's modelling

Contrary to 2D aerodynamics, in 3D aerodynamics the influence of the wake is important and thus, the created forces are affected by its geometry. For this reason, it is important to model in a correct way the wake based on several physical effects.

In order to determine the wake strength, the *Kelvin's theorem* is used, namely:

$$\frac{d\Gamma}{dt} = 0 \tag{3.63}$$

Kelvin's theorem states that: "The time rate of circulation around a closed curve consisting of the same fluid is zero". This is valid for any inviscid and incompressible fluid. Its derivation can be found in Chapter 2 of [16].

On the other hand , it has been explained in § 3.4.1 that the wake, similarly to the wing, is discretised into panels with a given circulation that are shed as the wing moves. Nonetheless, the wake is not a solid surface, like the wing; therefore, it cannot produce forces –i.e.: it cannot withstand a differential in pressure between the upper and lower surface. According to *Kutta-Joukowsky theorem*, the force a vortex filament produces is computed the following way,

$$\Delta p = \rho \boldsymbol{v} \times \gamma,$$

where ρ is the fluid density and γ is the vortex distribution per unit length. Hence, it can be concluded that $\Delta p = 0$ if

$$\boldsymbol{v} \parallel \gamma,$$

that means the wake is a stream surface; thus, it must move with the local velocity. This latter condition is achieved in the numerical code by computing the local velocity at each corner point of the wake panels and moving them with such velocity every time step. This is known as *wake roll-up*. Furthermore, by applying eq. (3.63), it is inferred that the circulation of the wake panels must remain constant.

In sight of the above, wake's modelling is carried out in the following way. At $t = 0$, the end of the latest wing's vortex ring correspond to the so-called *starting vortex* of the wing, as depicted in Figure 3.10a, with circulation $\Gamma_{TE,t=0}$. Of course, $\Gamma_{TE,t=0}$ is the circulation of the wing panel, and it is computed from eq. (3.61). At the next time step, $t = \Delta t$, the wing has moved a distance $\boldsymbol{x}_O = \boldsymbol{v}_O \Delta t$, and the first row of the wake's panels is formed by connecting the corners of the trailing edges' panels with those of the starting vortex. And, accordingly with *Kelvin's theorem*, the circulation is $\Gamma_{TE,t=0}$, as depicted in Figure 3.10b. That is why, it was stated that the circulation of the wake, Γ_k is known. Finally, the corner points are moved with the local fluid velocity so that the wake is a *force free* surface.

The end of the *trailing edge* panels' vortex ring is placed $0.3\, U_c\, \Delta t$ away from the trailing edge of the wing. The reasoning is related to 2D unsteady aerodynamics and can be found in Chapter 9 of [16].

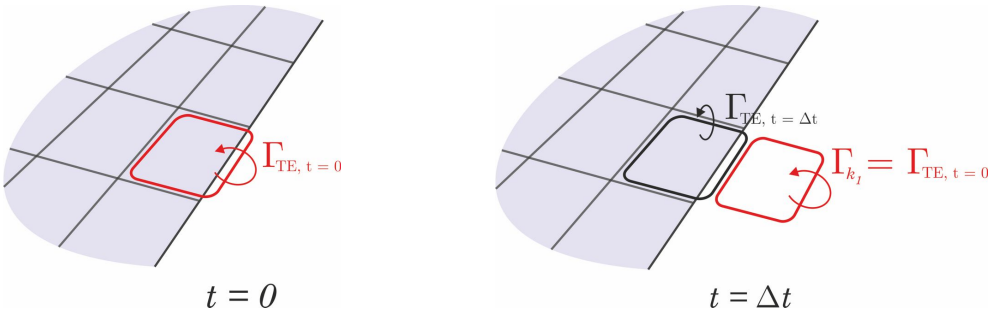

(a) Shed panel at $t = 0$ **(b)** Shed panel at $t = \Delta t$

Figure 3.10: Wake shedding procedure (TE stands for *trailing edge*).

In a real flow, the circulation of the wake decreases with time due to viscous dissipation or turbulence [20]. This vortex dissipation can be approximated in the potential model by different approaches (see, for example [20] and [21]). Nonetheless, since the influence in the results is minor, and its inclusion in the code increases the computational time, it is not added in the present code.

3.4.4 Forces computation

Normal Force

In order to compute the aerodynamic forces, eq. (3.55) is used to compute the pressure difference between the upper and lower surfaces of each wing panel. In this way, the total force normal to the wing is computed according to:

$$F_n = \sum_{i=1}^{i_N} \sum_{j=1}^{j_N} \Delta F_{n_{ij}} = \sum_{i=1}^{i_N} \sum_{j=1}^{j_N} \Delta p_{ij} \Delta x_{ij} \Delta y_{ij} \tag{3.64}$$

Where $\Delta p_{ij} = p_{l_{ij}} - p_{u_{ij}}$, being p_l and p_u the pressures on the lower and upper surfaces, respectively.

In order to express eq. (3.55) in terms of circulations, Γ_{ij}, it has to be rewritten. To ease this task, it is written below:

$$p = p_\infty + \frac{1}{2}\rho\|\boldsymbol{v}\|^2 - \frac{1}{2}\rho\|\boldsymbol{v}_{rel}\|^2 - \rho\dot{\phi} \tag{3.55}$$

First, one must notice that $\|\boldsymbol{v}_{rel}\|^2$ is equal to:

$$\|\boldsymbol{v}_{rel}\|^2 = (\boldsymbol{v}_{rel} \cdot \boldsymbol{n})^2 + (\boldsymbol{v}_{rel} \cdot \boldsymbol{\tau}_x)^2 + (\boldsymbol{v}_{rel} \cdot \boldsymbol{\tau}_y)^2,$$

being τ the unitary vector in x and y directions, in accordance to Figure 3.8 (the unitary vectors $\boldsymbol{i}$ and $\boldsymbol{j}$ have not been used to avoid confusion with the panel indexers). By definition, $\boldsymbol{v}_{rel} \cdot \boldsymbol{n} = 0$. Furthermore:

$$\boldsymbol{v}_{rel} = \nabla\phi - \boldsymbol{V}_p$$

Notice that capital V has been used since $\boldsymbol{V}_p$ is the rigid body velocity of the point, namely, $\boldsymbol{V}_p = \boldsymbol{v}_O + \boldsymbol{\Omega} \times \boldsymbol{x}'_p$. In turn:

$$\nabla\phi = \nabla\phi_w + \nabla\phi_k.$$

In sight of the above, and after some algebra, the pressure difference for a given panel takes the form:

$$\Delta p = \rho \left[(\boldsymbol{V}_p - \nabla\phi_k)_{\tau_x} \left(\left.\frac{\partial\phi_w}{\partial\tau_x}\right|_u - \left.\frac{\partial\phi_w}{\partial\tau_x}\right|_l \right) + (\boldsymbol{V}_p - \nabla\phi_k)_{\tau_y} \left(\left.\frac{\partial\phi_w}{\partial\tau_y}\right|_u - \left.\frac{\partial\phi_w}{\partial\tau_y}\right|_l \right) + \dot{\phi}_u - \dot{\phi}_l \right] \tag{3.65}$$

In eq. (3.65), the subscript τ stands for the corresponding vector component. Eq. (3.65) does not relate pressure difference with circulation. To that end, one has to realize, from potential aerodynamics, that velocity at a point $z = \pm 0$, which is induced by a vortex distribution placed at $z = 0$, is:

$$u(x, y, 0^+) = \frac{\partial\phi}{\partial x}(x, y, 0^+) = \frac{\gamma_y}{2} \tag{3.66}$$

$$u(x, y, 0^-) = \frac{\partial\phi}{\partial x}(x, y, 0^+) = -\frac{\gamma_y}{2} \tag{3.67}$$

The same reasoning is applied v (Being $\boldsymbol{v} = (u, v, w)$). Therefore, the terms:

$$\left.\frac{\partial\phi_w}{\partial\tau}\right|_u - \left.\frac{\partial\phi_w}{\partial\tau}\right|_l,$$

of eq. (3.65), turns out to be:

$$\left.\frac{\partial\phi_w}{\partial\tau_x}\right|_u - \left.\frac{\partial\phi_w}{\partial\tau_x}\right|_l = \gamma_y,$$
$$\left.\frac{\partial\phi_w}{\partial\tau_y}\right|_u - \left.\frac{\partial\phi_w}{\partial\tau_y}\right|_l = \gamma_x.$$

In turn, by definition:

$$\gamma_y = \frac{d\Gamma}{dx}, \qquad \gamma_x = \frac{d\Gamma}{dy}. \tag{3.68}$$

On the other hand, time derivatives of eq. (3.65) can be rewritten, by means of eqs. (3.66), (3.67) and (3.68), as:

$$\dot{\phi}_u - \dot{\phi}_l = \frac{\partial}{\partial t}\int_0^x \frac{\gamma_y}{2}\,dx \; - \; \frac{\partial}{\partial t}\int_0^x -\frac{\gamma_y}{2}\,dx = \frac{\partial \Gamma}{\partial t} \tag{3.69}$$

Finally, the pressure jump at a given point is expressed as:

$$\Delta p = \rho\left[(\boldsymbol{V}_p - \nabla\phi_k)_{\tau_x}\frac{d\Gamma}{dx} + (\boldsymbol{V}_p - \nabla\phi_k)_{\tau_y}\frac{d\Gamma}{dy} + \frac{\partial\Gamma}{\partial t}\right] \tag{3.70}$$

Upon discretization it can be shown that, for a given panel with indexes i, j, the pressure jump is:

$$\Delta p_{ij} = \rho\left[(\boldsymbol{V}_p - \nabla\phi_k|_{ij})_{\tau_{x_{ij}}}\frac{\Gamma_{i,j} - \Gamma_{i-1,j}}{\Delta x_{ij}} + (\boldsymbol{V}_p - \nabla\phi_k|_{ij})_{\tau_{y_{ij}}}\frac{\Gamma_{i,j+1} + \Gamma_{i,j+1}}{2\Delta y_{ij}} + \frac{\partial\Gamma_{i,j}}{\partial t}\right] \tag{3.71}$$

Tangential Force

The computation of tangential forces is an elusive goal for vortex panel methods. First of all, since the method is potential, tangential forces due to viscous stresses cannot be computed. Similarly, since the wing is infinitely thin, neither the suction peak at the leading edge can be computed. For these reasons, in the existing literature, vortex methods are commonly used to compute only normal forces, as in [22]. Even though there are attempts to characterize the suction peak at the leading edge based on analytical solutions from potential aerodynamics, these solutions are based on the steady case of a 2D flat plate at given angle of attack (see [23]). Therefore, their use does not fit with the envisaged purpose of the present study.

Despite the previous fact, [16] introduces a method for calculating the induced drag –then, the force is parallel to the free stream–, of a wing that is suddenly accelerated. In a similar way to the normal force contribution, the induced drag is owed to two contributions; the first one is due to the wake-induced downwash; and the second one is due to the fluid acceleration. Following this approach, and for a wing that moves with a given angle of attack, parallel to the x *axis* of Σ_I with a velocity $\boldsymbol{v}_O = -U\boldsymbol{i}_I$, the induced drag takes the form:

$$\Delta D_{ij} = \rho\left[w_{ind_{ij}}(\Gamma_{i,j} - \Gamma_{i-1,j})\Delta y_{ij} + \frac{\partial\Gamma_{i,j}}{\partial t}\Delta x_{ij}\Delta y_{ij}\sin\alpha_{ij}\right] \tag{3.72}$$

In eq. (3.72), $w_{ind_{ij}}$ is the velocity perpendicular to the free stream –i.e.: U– that is induced by the wake vortices and the chordwise vortices of the wing (following

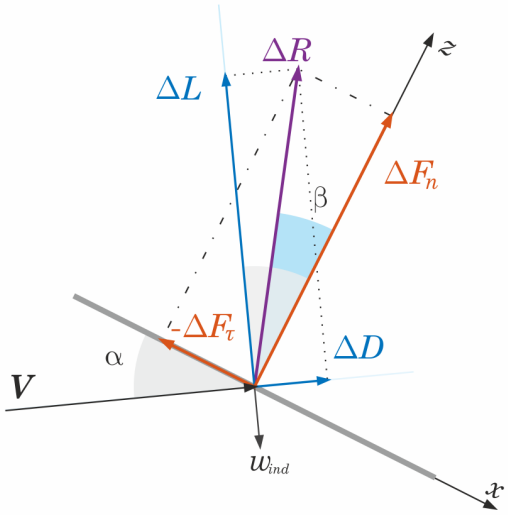

Figure 3.11: Forces diagram on a wing panel

Prandtl's Lifting Line model); and α_{ij} is the angle that the panel forms with the free stream.

The disadvantage of the previous formulation is that it is only applicable when the wing has no angular velocity. Otherwise, from eq. (3.4), the *free stream* velocity seen by each panel is different, both in magnitude and direction. In order to solve this, a formulation is proposed in this project, to determine the tangential force, F_τ, based on eqs. (3.71) and (3.72) and the definitions of Lift and Drag, and Normal and Tangential forces. In this fashion, the decomposition of forces for a given panel is displayed in Figure 3.11. Where $\boldsymbol{V}_{ij}$ is the kinematic velocity of the panel, as given in eq. (3.4); and ΔR is the resultant force at the panel. Looking at Figure 3.11 it is straightforward to notice that:

$$\begin{aligned} \Delta F_n &= \Delta R \cos\beta \\ \Delta D &= \Delta R \sin(\alpha - \beta) \end{aligned}$$

ΔF_n and ΔD are known from eqs. (3.64) and (3.72). Similarly, α can be obtained from the kinematic velocity. Thus, the only unknowns are ΔR and β. After some algebra and making use of trigonometric relationship it is possible to show that:

$$\beta = \tan^{-1}\left(\frac{\Delta D}{\Delta F_n \cos\alpha} - \tan\alpha\right) \tag{3.73}$$

Now, ΔR can be computed from any of the two previous equations; and conse-

quently, ΔF_τ is obtained from:

$$\Delta F_\tau = -\Delta R \sin\beta \tag{3.74}$$

If this process is repeated for every panel of the wing, the total tangential force is obtained straightforward as:

$$F_\tau = \sum_{i=1}^{i_N} \sum_{j=1}^{j_N} \Delta F_{\tau_{ij}} \tag{3.75}$$

3.4.5 Formulation for two wings

The previous algorithm was implemented for one wing as a first step in the project. However, to complete the objectives of the project, it was necessary to develop a version of the code with two wings. The corresponding modifications of the algorithm are presented in this section.

First, it must be noticed that each wing has an influence on the flow around the other. This must be taken into account whenever the fluid velocities near one wing are computed. In this fashion, the determination of the circulation, and the calculation of the forces are modified. Similarly, the same considerations are applied to the wakes left by both wings.

Eq. (3.39) must be applied to both wings and the influence of the other wing has to be taken into account. Therefore, for a control point of the left wing, eq. (3.39) becomes:

$$\sum_{l=1}^{N_{w_L}} a_{l_L} \Gamma_{l_L} + \sum_{l=1}^{N_{w_R}} b_{l_{R\to L}} \Gamma_{l_R} + \nabla\phi_k \cdot \boldsymbol{n} = \boldsymbol{V}_p \cdot \boldsymbol{n} \tag{3.76}$$

In eq. (3.76), subscript L stands for left wing, and R for right wing. Hence, a_{l_L} is the influence coefficient of l panel on the given control point; $b_{l_{R\to L}}$ is the induced velocity on the control point by l panel on the right wing if Γ_{l_R} was 1. Note that, although there are two wakes, their contribution has been included a single term, since their circulation is known. Likewise, for the right wing:

$$\sum_{l=1}^{N_{w_L}} b_{l_{L\to R}} \Gamma_{l_L} + \sum_{l=1}^{N_{w_R}} a_{l_R} \Gamma_{l_R} + \nabla\phi_k \cdot \boldsymbol{n} = \boldsymbol{V}_p \cdot \boldsymbol{n} \tag{3.77}$$

At first glance, it seems a system of matrices with 2 unknown vectors. However, following the same approach than in § 3.4.2, a single system can be constructed. Namely:

$$\left(\begin{array}{c|c} A_L & B_{R\to L} \\ \hline B_{L\to R} & A_R \end{array}\right)\begin{pmatrix}\vec{\Gamma}_L \\ \vec{\Gamma}_R\end{pmatrix} = \begin{pmatrix} R\vec{H}S_L \\ R\vec{H}S_R\end{pmatrix}, \tag{3.78}$$

where A and B are the matrices of the influence coefficients as appearing in eq. (3.61). The upper arrow has been used to emphasize that Γ and RHS are column vectors. The advantage of eq. (3.78) is that it is easily solved using MATLAB®.

Two things must be taken into account when computing the influence coefficients of the matrix B. Firstly, the relative position of the wings is changing with time; thus, the influence coefficients will have to be computed for each time step. Secondly, the transformation between reference frames explained in § 3.2.3 must be applied, since each wing has its own reference frame, i.e.: Σ_{w_L} and Σ_{w_R}. On the other hand, for the computation of forces, the velocities induced by the other wing and the wake must be included.

Chapter 4

Validation

Based on the theory explained in the previous chapter, two numerical codes have been developed using MATLAB®. The principal code, which is the main objective of the present project, is called *AeroFlaps*. It computes the aerodynamic forces produced by two wings that move with an imposed motion. On the other hand, as a first step in the project, an algorithm with only one wing –named *OneWing*–, was developed with the aim of validating the codes with the present algorithm.

Therefore, in this chapter several cases are presented to validate the codes. This chapter starts with the validation of *OneWing*, which can be validated directly with the results of [16]. On the other hand, since cases that can be directly compared to *AeroFlaps* have not been found, the validation of *AeroFlaps* is based on several comparisons with *OneWing*. Nonetheless, *AeroFlaps* is an extension of *OneWing*.

4.1 Sudden Acceleration of a flat plate

In Section 13.12 of [16], the case of a *Sudden Acceleration of an Uncambered Rectangular Wing into a Constant-Speed Forward Flight* is presented. Several *Aspect Ratio*[1] are studied. The angle of attack is set equal to $\alpha = 5°$. Therefore, by setting the point O to coincide with I, the kinematic equations explained in § 3.2.4 yields

$$\boldsymbol{v}_O^I(t) = (-U_\infty, 0, 0),$$

and the Eulerian angles

$$\varphi(t) = 0, \qquad \theta(t) = \alpha, \qquad \psi(t) = 0.$$

[1] The *Aspect Ratio*, is defined as the ratio between the span, b, and the chord, c, of the wing: $AR = b/c$.

Thus, $\mathbf{\Omega}(t) = (0, 0, 0)$.

In eq. (3.62), $U_c = U_\infty$, and the wing's discretization is $i_N = 4$ and $j_N = 26$.

In Figure 4.1, the simulation of the sudden start using *OneWing* is shown. The caption corresponds to the instant when $X_0 = -16c$. One can observe how the starting vortex has formed and rolled, and the roll up of the wake at the tips.

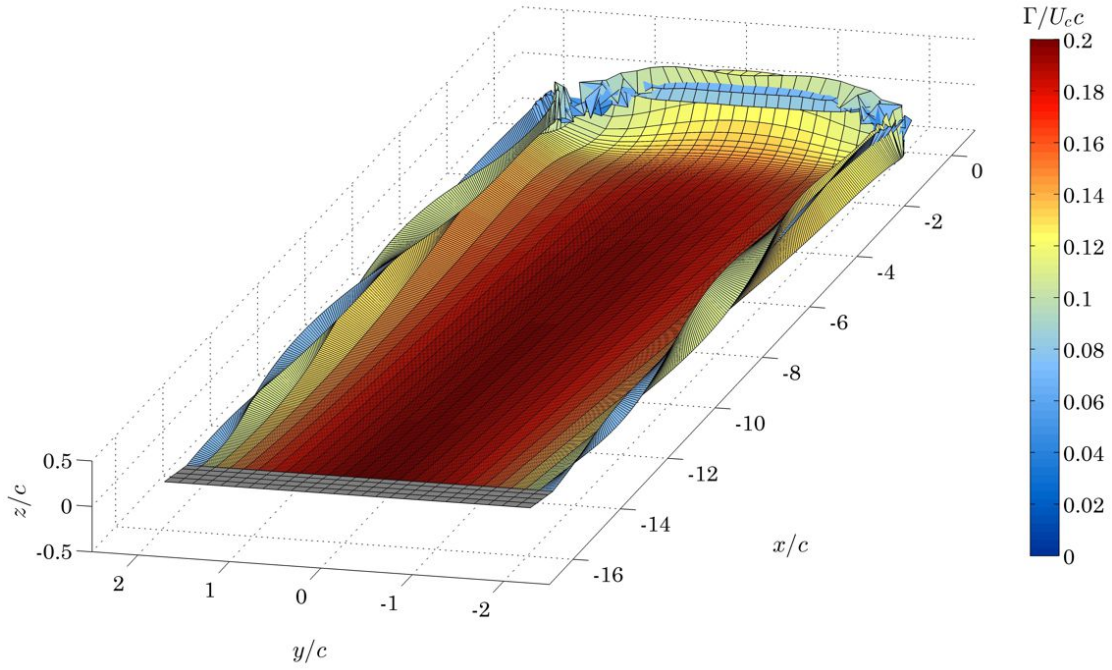

Figure 4.1: Uncambered Wing into a Constant-Speed Forward Flight using *OneWing*. Distance travelled, $X_0 = -16c$; $\alpha = 5°$.

4.1.1 Normal Force

Figure 4.2 shows the evolution of F_n with time under the previous conditions. Notice that F_n has been adimensionalised according to:

$$C_n = \frac{F_n}{\frac{1}{2}\rho U_\infty^2 c}$$

Data in [16] has been extracted directly from a graph using a digitalizing software. There, one can appreciate the results obtained using *OneWing* and those of [16]. One can observe that the results of *OneWing* coincide with those expected from [16].

Regarding the results in Figure 4.2 several observations can be made. First of all, it is observed in the first time step a large force produced by the absence of the trailing wake. After that, the force largely decreases due to the development of the *starting vortex*. As time evolves, the unsteady contribution to the normal force decreases until a steady value of C_n is reached. Note also that, as expected, C_n is higher for the wings with larger AR.

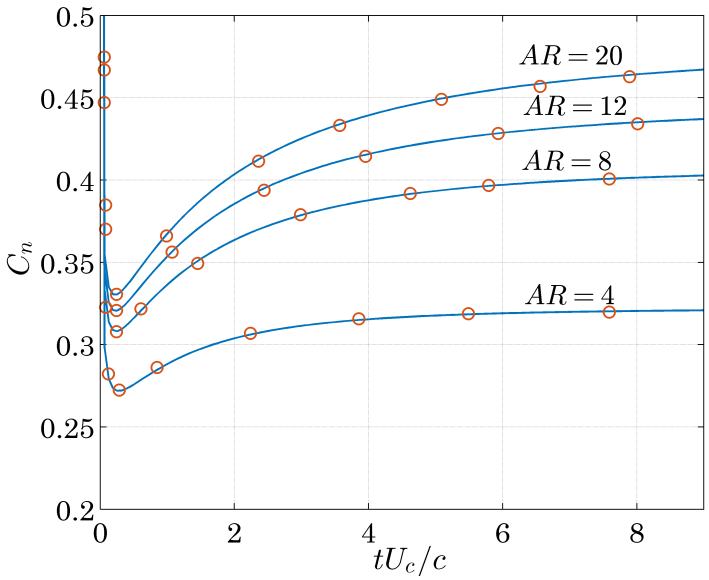

Figure 4.2: Sudden Acceleration: Normal force coefficient, C_n, versus nondimensional time. (○) Data from Ref. [16]; (—) *OneWing*.

4.1.2 Induced Drag

It was commented in § 3.4.4 that Ref. [16] computes the induced drag using the induced velocity that is normal to the freestream direction. On the contrary, the developed code, based on the previous approach, computes the normal and tangential force on the wing. Since the results available in [16] are referred to the induced drag, the tangential and normal forces calculated using *OneWing* have been projected to the inertial x *axis*. The comparison between both methods is presented in Figure 4.3.

Regarding the results in Figure 4.3, one can appreciate that the induced drag coefficient increases as the AR decreases. Of course, this is due to the higher influence of the trailing vortices at the wing tips for wings with lower AR. The argument between both methods is satisfactory.

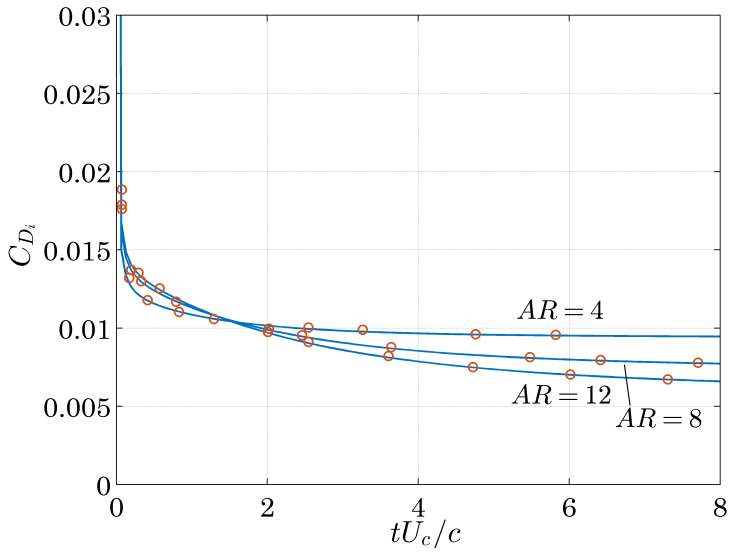

Figure 4.3: Sudden Acceleration: Induced Drag coefficient, C_{D_i}, versus nondimensional time. (○) Data from Ref. [16]; (—) *OneWing*.

4.2 Flat plate in heaving

Another case found in [16] to validate *OneWing* is the *Heaving Oscillations of a Rectangular Wing*. A planar rectangular wing with $AR = 4$ is simulated. The angle of attack of the wing is $\alpha = -5°$ and the heaving amplitude is $h_0 = 0.1c$. Hence, the kinematics of the wing is

$$X_0 = -U_\infty t, \qquad Y_0 = 0, \qquad Z_0 = h_0 \sin \omega t.$$

Hence, $\boldsymbol{v}_O^I(t) = (-U_\infty, 0, h_0\omega \cos \omega t)$. Likewise,

$$\varphi(t) = 0, \qquad \theta(t) = \alpha, \qquad \psi(t) = 0.$$

In the previous equations, ω (with units: rad/s) defines the heaving frequency[2]. At this point it is useful to the define the so-called *reduced frequency*, k. It relates the horizontal and vertical velocities by the following equation:

$$k = \frac{\omega}{U_\infty/c} \tag{4.1}$$

The simulation is performed with $k = 1$. In order to determine the required time step, one must take into account that the wing moves with both horizontal and

[2]By definition $\omega = 2\pi f$, being f the frequency (units $1/t$).

vertical velocity. If Δt is computed using U_∞, the step size is larger; thus, the distance between wake shed points when the wing's velocity is maximum can be too large. For that reason, U_c in eq. (3.62) is chosen to be the maximum velocity, namely:

$$U_c = \sqrt{U_\infty^2 + (h_0\omega)^2} \tag{4.2}$$

Nonetheless, in the force adimensionalization, U_∞ is used. The number of wing panels used in [16] is unknown since only the plot is presented as an example of application, referring to [24] for detailed info. However, the author of the present project has not been able to access to [24]. Therefore, it is decided to choose the same number of panels than in § 4.1.

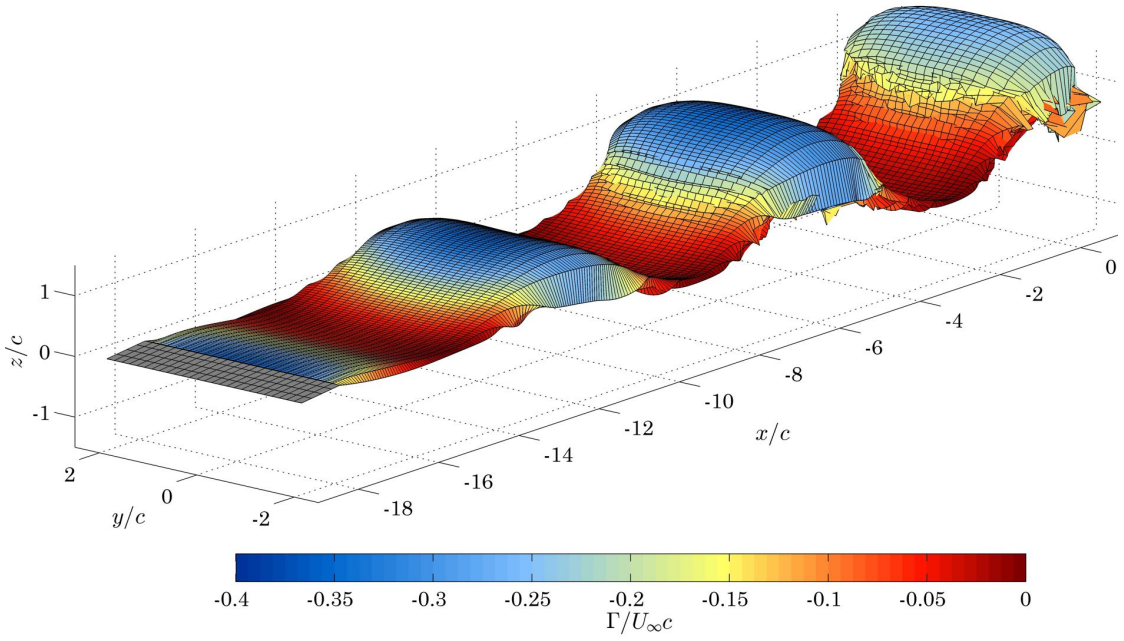

Figure 4.4: Uncambered Wing in heaving motion using *OneWing*. $h_0 = 0.1c$; $k = 1$; $\alpha = -5°$.

In Figure 4.4 a simulation of 3 periods perfomed with *OneWing* is displayed. It is remarkable that the wake's roll up that is produced by the wake itself (notice the initial wake elements have displaced from $0.1h_0$ to h_0 upwards). The comparison of the forces is sketched in Figure 4.5. The plot from [16] provides one period (not a time history); thus, the comparison is done with the third period of the simulation, since it is assumed that the results are closer to a steady result. Contrary to previous validations, it is observed that the comparison is not exact. However, it is considered satisfactory due to the previous mentioned reasons: the number of panels is unknown, so is the corresponding period and the selected Δt. Besides,

the wake's roll up may influence: while *OneWing* computes the wake's roll up with the whole wake, code from [16] moves only the five latest shed vortices, while the older wake vortices remain fixed.

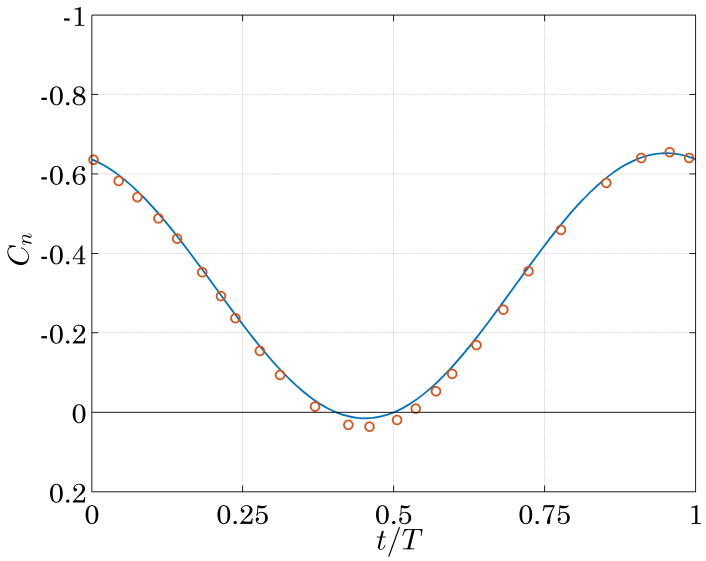

Figure 4.5: Heaving Oscillations: Normal force coefficient, C_n, versus nondimensional time. (○) Data from Ref. [16]; (—) *OneWing*.

4.3 Two wings: *AeroFlaps*

As commented before, the author has not been able to find cases in the literature to directly validate *AeroFlaps*. However, since it is an improved and extended version of *OneWing*, several cases can be run, once *OneWing* is validated, to compare the results. In this fashion, the following cases has been tested:

Two wings separated by a large distance. If the distance between the two wings is set large enough, the aerodynamic forces produced by each wing should be similar to those produced by a single wing. In this fashion, a distance $d = 20c$ between the two wings –with $AR = 4$– is set and a sudden start is simulated. It is seen that, in fact, the aerodynamic forces developed by each wing were similar to those obtained in § 4.1. The results are not displayed because the difference in the result is too small to be perceived in a graph. Particularly, the wing circulation of both cases were compared, yielding a maximum relative error of the order of 10^{-5}.

Two wings joined at the tips. Contrary to the previous case, if $d = 0$, the two wings should behave as a single wing with twice the span of each wing. Following this line of thought, a sudden start and a heaving motion is performed using wings with $AR = 2$ and $d = 0$. The results match exactly (except for numerical errors, of the order of 10^{-17}) with those of § 4.1 and § 4.2.

4.4 Effect of the wake

When discussing the results in § 4.1 and 4.2, the influence of the wake in the resulting forces has been noted. Furthermore, in an unsteady motion, the wake acts as the historical record of the motion. Nonetheless, as the wings travel, the distance from a given wake element increases and, consequently, the influence of such element on the wings decreases. For that reason, it should be possible to neglect the influence of such elements without significantly modifying the resulting aerodynamic forces.

By neglecting points of the wake, the computational cost decreases and the computing time can be reduced. This is specially advantageous when it is required to perform long time simulations. An example of this is found in [15]: in this thesis, an algorithm similar to *OneWing* was implemented to study the effect of unsteady aerodynamics in a dynamic model of a MAV. Therefore, long time simulations (of the order of $16,000c$) were needed, which would be unbearable to perform with all the wake elements due to the computational cost and the required memory space.

In view of the above, a study was performed to determine the number of wake panels that are required to keep the error in the forces small enough. To that end, several analyses have been performed, as discussed below.

Sudden Acceleration

The steady state forces of a sudden acceleration for different wake lengths are compared. The same parameters as in § 4.1 are used; the aspect ratio of the wing is $AR = 4$; and it is assumed a steady state is achieved when $X_0 = -12c$ (at this state, variations in the forces are of the order of 10^{-6}). Four different wake lengths, w_L, are compared with the full length case, namely: $1c$, $2c$, $4c$ and $8c$ (when talking about *wake length*, it is assumed the length is equal to the distance X_0 travelled by the wing). Thus, w_L is imposed to one of the previous values and the case is run until $X_0 = -12c$; then, the forces are compared and the error is computed using eq. (4.3). Namely:

$$\varepsilon = \frac{C_{n_{w_L=12c}} - C_{n_{w_L=Xc}}}{C_{n_{w_L=12c}}} \tag{4.3}$$

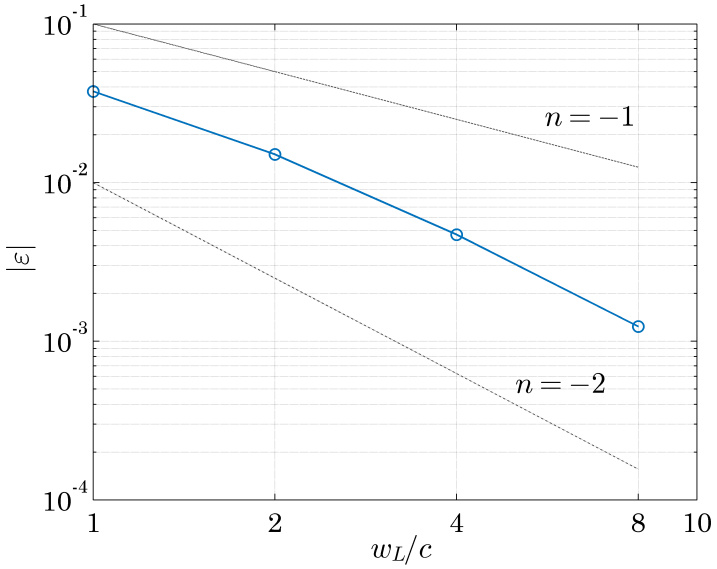

Figure 4.6: Effect of the wake length in the forces (Uncambered rectangular wing into a Constant-Speed Forward Flight).

In Figure 4.6 the error in the forces versus w_L is displayed, where it can be observed that the error decreases as w_L increases, as expected. Two additional lines are depicted, corresponding to functions of the shape $f(x) = kx^n$, showing that the decrease in the error is between $n = -1$ and $n = -2$.

Heaving

The same procedure is followed for a heaving motion. Based on case from § 4.2, ε is computed for different wake lengths. However, since a steady value is not reached, the comparison cannot be performed for a single value, instead the error history is depicted (see Figure 4.7). The same tendency is observed, i.e.: the error decreases as w_L increases. To better illustrate this behaviour, the mean value of $|\varepsilon|$ has been calculated for each w_L and it is depicted in Figure 4.8.

From the previous study, it was determined that a suitable w_L for the purpose of [15] is $w_L = 5c$, yielding an error between 0.1% and 1%.

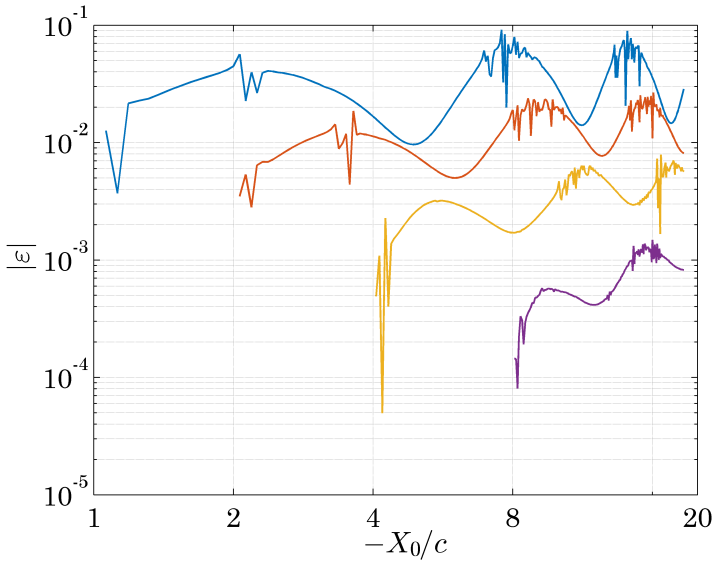

Figure 4.7: Error variation (Heaving Oscillations). (—) $w_L = 1c$; (—) $w_L = 2c$; (—) $w_L = 4c$; (—) $w_L = 8c$.

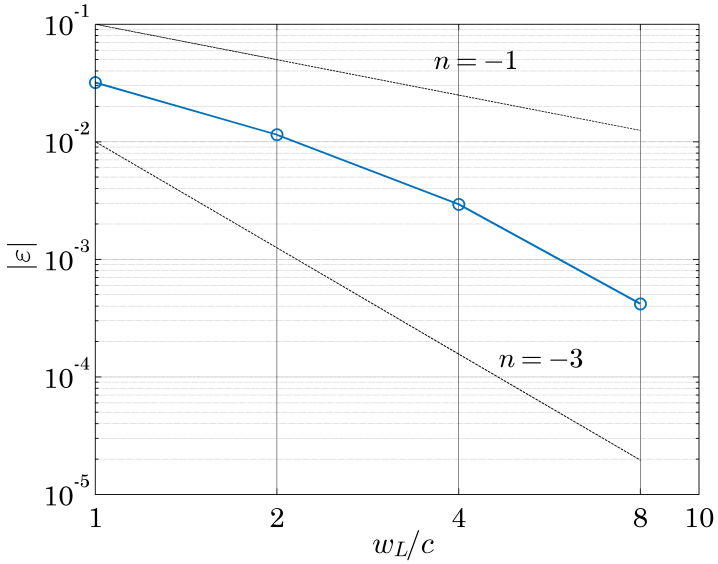

Figure 4.8: Effect of the wake length in the forces (Heaving oscillations).

Chapter 5

Results

The previous chapter dealt with code validation. To that end, cases in which potential theory hold –i.e.: low angles of attack and small heaving amplitudes– were analysed. However, the main objective of this project is the computation of aerodynamic forces for flapping motion which generally has, as commented before, high angles of attack and amplitudes. For that reason, in this chapter, two cases corresponding to these kind of motions are analysed. The first case of study corresponds to the pitching of a wing whose forces are measured experimentally. The second case is a comparison with a high-order NS code for the high amplitude heaving of two wings. Finally, a study of the performance of two wings in flapping motion is assessed. To that end, the aerodynamic performance for different flapping radii is studied.

5.1 Pitching oscillations of a wing in a Uniform Stream

In [25] experimental forces of a pitching rigid flat plate moving with a uniform velocity inside a water tank are measured. Pitching motion takes place at high amplitude and with a high reduced frequency. Therefore, this experiment is very suitable to assess the accuracy of the developed codes to compute forces.

Pitching motion is a simple sinusoidal function of the form:

$$\theta(t) = \theta_0 \sin \omega t \tag{5.1}$$

Y-axis of Σ_w is set to coincide with the leading edge of the wing, so that the

pitching axis is the leading edge. Hence, the kinematics equations turn out to be:

$$\boldsymbol{v}_O^I = (-U_\infty, 0, 0), \qquad \boldsymbol{\Omega}^w = (0, \theta_0 \omega \cos \omega t, 0).$$

The aspect ratio of the flat wing is $AR = 1.667$; the pitching amplitude is $\theta_0 = 24°$; and the reduced frequency is $k = 6.75$ (Notice that values of θ_0 and k are several times greater than those of Chapter 4). The *Reynolds number* at which the experiment is performed is $Re = 14 \cdot 10^4$.

For the simulation *OneWing* is used. The number of wing panels is $i_N = 4$ and $j_N = 26$; and in order to compute Δt, the characteristic velocity is set to be the maximum velocity at the trailing edge:

$$U_c = \sqrt{U_\infty^2 + (c\theta_0\omega)^2}$$

Ref. [25] provides the time history of the forces that are measured experimentally in the inertial reference frame. Hence, forces are computed according to:

$$C_Z = C_n \cos\theta - C_\tau \sin\theta$$
$$C_X = C_n \sin\theta + C_\tau \cos\theta$$

Comparison of the forces is depicted in Figure 5.1. Regarding the forces perpendicular to the freestream velocity (Figure 5.1a), it can be observed that the unsteady potential method accurately predicts the forces until flow separation is produced in the real model, causing a decrease in the forces.

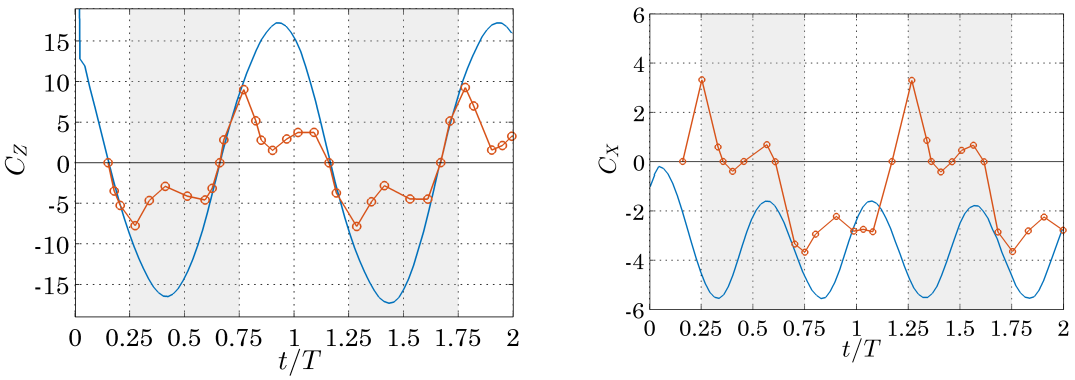

(a) Vertical Force

(b) Horizontal Force

Figure 5.1: Force coefficients vs. nondimensional time. Shaded regions correspond to the upstroke while white regions correspond to the downstroke. $k = 6.75$ and $\theta_0 = 24°$. (—) *OneWing*; (—) Ref. [25].

Previous discrepancy in the forces is common in potential models since the flow is forced to remain attached to the wing. Therefore, the required circulation at the wing to fulfil the *zero normal flow* boundary condition is high, due to the large normal velocities at the wing's surface, yielding high differences in pressure. Although there are attempts to simulate flow separation by shedding vortex panels where separation occurs (e.g.: [22], [26] or [27]), they are based on empirical data to and 2D aerodynamics; and thus, they are not reliable for a general approach.

Regarding forces parallel to the freestream, one can observe in Figure 5.1b that results do not fit. On the one hand, the results from *OneWing* are expected since the flow must remain attached. This causes a large suction force tangential to the wing, which is the main contributor to C_X. In addition, it has to be considered that skin friction is not computed. Thus, a higher thrust force is produced. On the other hand, X oriented forces from Ref. [25] are expected to be equal during the upstroke, ($t = [0.25T, 0.75T]$) and the upstroke ($t = [0.75T, 1.25T]$) as the movement is symmetric. This is in fact what happens with results (see Figure 5.1b) from *OneWing*. However, this tendency is not observed in the results of Ref. [25], as seen in Figure 5.1. For that reason we have tried to contact the authors but we have had no response yet.

In Figure 5.1 the unsteady character of the motion is also noticed. For very low k (less than 0.1), the peak force is expected to occur when pitch angle is maximum. However, for high reduced frequencies, the peak force is linked to the angular velocity, which is maximum when $\theta = 0$. In Figure 5.1 one can observe the peak force occurs before this instant. This phase shift is due to fluid acceleration. Such contribution is captured by the time dependant term in pressure computation and the wake. One must take into account the wake has a large influence since at every stroke, a high intensity vortex is left, and since horizontal wing displacement is small compared to vertical one, this vortex remains near the wing (this figure is clearly sketched in Figure 5.2). The effect of this vortex is to induce a downward velocity on the plate, thus, lowering the normal velocity the wing sees.

High order models, are capable of showing the vorticity of the fluid elements. However, in a potential model this is not possible since only the points of the wake are modelled –not the entire fluid domain– and the vorticity is zero outside the infinitely thin wake. Nevertheless, an approach to display the circulation inside a plane is made in the present project. To that end, a given plane is selected and the position and intensity of the vortex lines belonging to the wake that passes through it are computed. Then, the vorticity is represented as shown in Figure 5.2 (corresponding to the plane $y = 0$), where the flow velocity is also sketched. In Figure 5.2, the intensity of the circulation is also represented by the radius of the vortex element represented. One can observe the roll-up of the last vortices due to the downstroke as well as the suction peak at the leading edge. It

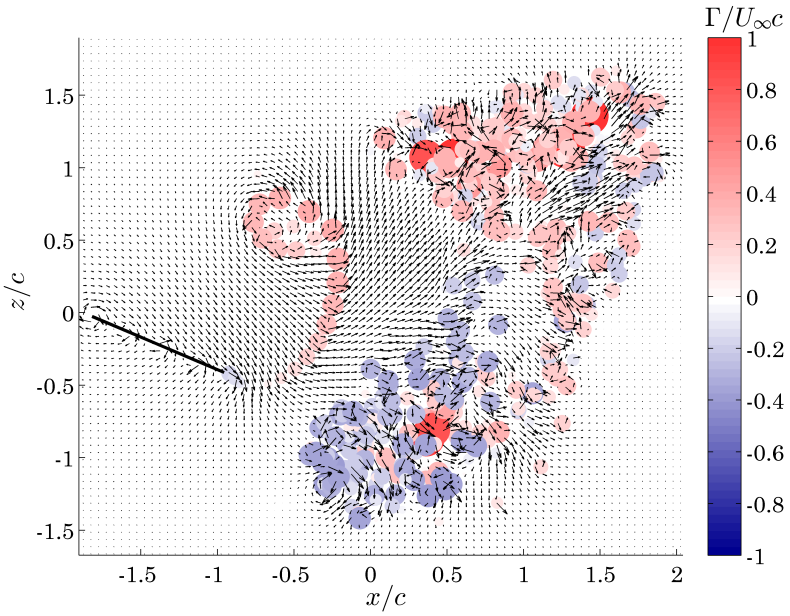

Figure 5.2: Vorticity representation at the beginning of the upstroke, cutting plane $y = 0$ (Γ is considered to be positive clockwise).

should be highlighted that the wake elements corresponding to the first stroke are highly entangled as compared to heaving simulation of § 4.2. This is due to the high reduced frequency of the present case: the horizontal displacement is small compared to the vertical displacement, specially at the trailing edge. Hence, the wake elements are too close to one another and the induced velocity they induce to one another is high, resulting in a highly deformed wake. A 3D representation of the wake after 2 periods is displayed in Figure 5.3.

5.2 Two wings in heaving

In the present section, normal and tangential forces of two wings in heaving are presented. A large heaving amplitude, h_0, is imposed; thus, fluid separation in a real case should be expected. In order to assess the accuracy of the results, they are compared to the ones obtained using TUCAN3, an immersed boundary, Navier-Stokes solver developed in the CFD Lab of the Bioengineering and Aerospace Engineering Dept. of the UC3M (http://aero.uc3m.es/cfd.html).

Each wing has an $AR = 2$; the distance between them is $d = 0.5$; the heaving amplitude is $h_0 = 1c$; and the reduced frequency is $k = 1$. The wings are moving with a forward velocity U_∞. In order to determine Δt from eq. (3.62), the same

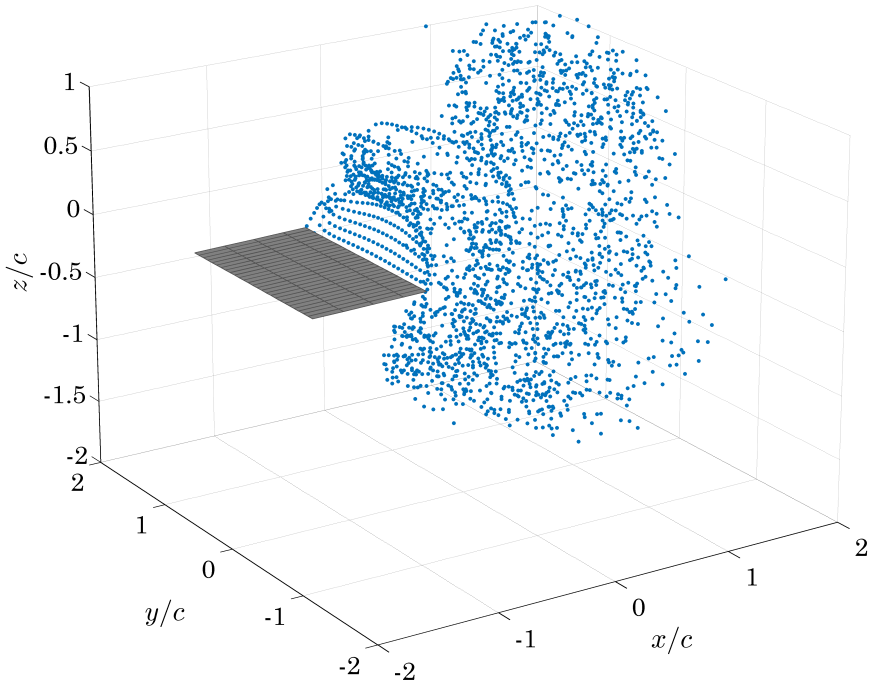

Figure 5.3: Wing panels and wake points at $t = 2T$ ($\theta_0 = 24°$ and $k = 6.75$).

characteristic velocity, U_c, that the one defined in § 4.2 is used. For the high order NS model, a *Reynolds number* equal to $Re = 100$ is selected. Note that in this regime, viscous effects become important. In the potential code, each wing is discretized into $i_N = 4$ and $j_N = 15$ panels. On the other hand, wings modelled with TUCAN3 have finite thickness of $0.125c$. The wings are discretized into 9792 points (both wings included). Regarding the fluid domain, it consists of $[230 \times 190 \times 270]$ points. The kinematic equations of the motion are those of § 4.2.

The results are depicted in Figure 5.4. The coefficients have been computed according to: $C_{n,\tau} = C_{n,\tau_L} + C_{n,\tau_R}$. First of all, it can be observed a perfect agreement regarding normal forces (Figure 5.4a). On the contrary, tangential forces do not coincide (Figure 5.4b). Whereas, *AeroFlaps* predicts a net thrust (Note the wings are always parallel to the streamwise velocity), TUCAN3 predicts the wings are always producing drag. This discrepancy is expected, since *AeroFlaps* does not take into account skin friction and it assumes there is no separation. Hence, in the end, only the suction force is computed.

Discussing the results several appreciations can be made. In Figure 5.4a, one can observe normal force is maximum near $t = 0.5T$, when wings have maximum downwards velocity; and minimum near $t = 1T$, when upwards velocity is maxi-

mum. Similarly, in Figure 5.4b, it can be appreciated that tangential force is near 0 in the potential case at the beginning of the upstroke and the downstroke, where the vertical velocity is small. On the contrary, when vertical velocity is high, suction force is high, both at the upstroke and the downstroke, since as previously commented, the flow must remain attached.

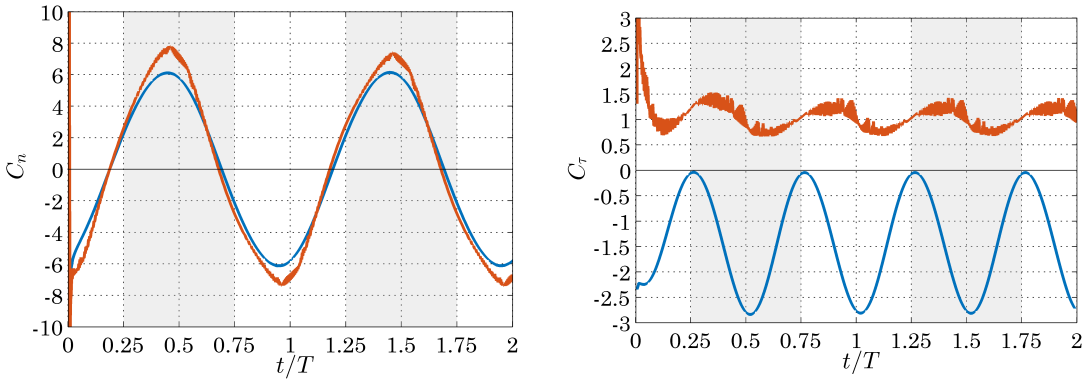

(a) Normal force. **(b)** Tangential force.

Figure 5.4: Force coefficients vs. non dimensional time (Heaving motion). $h_0 = 1c$; $k = 1$. (—) *AeroFlaps*; (—) High-Order NS model, $Re = 100$.

In order to better discuss the results, the suction force is compared. To that end, the force contribution of the leading edge wings' elements is added (recall the wings simulated in TUCAN3 have finite thickness). The projection of such forces along x *axis* corresponds to the suction force. In Figure 5.5, the comparison of suction forces is displayed. There, it can be appreciated a similar behaviour, but a smaller suction force in the case of results from TUCAN3, probably due to fluid separation.

From the discussion above, it can be concluded that *AeroFlaps* accurately computes normal forces to the wings in a heaving motion with high amplitude. Tangential forces cannot be predicted, since neither separation nor skin friction is computed. Therefore, *AeroFlaps* always predicts thrust generation. Nevertheless, it is worth to mention that, while TUCAN3, running with 32 processors takes around $1,700\,min$ to simulate 2 periods, *AeroFlaps* running with a single processor, takes only $10\,min$. Thus, *AeroFlaps* turns out to be a very fast and suitable algorithm to compute forces normal to the plate –which normally result in lifting forces.

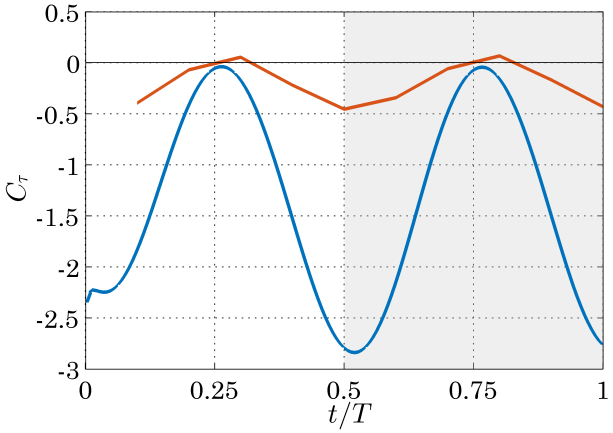

Figure 5.5: Tangential force vs. nondimensional time (Suction force). $h_0 = 1$; $k = 1$. (—) *AeroFlaps*; (—) High-Order NS model, $Re = 100$.

5.3 Analysis of Two Wings in Flapping

In this section, a study of the aerodynamic performance of two wings in flapping is presented. The main objective of this study is to investigate the effect of the flapping radius and to compare the differences between flapping and heaving. *AeroFlaps* is used for this purpose.

Since the main goal of this analysis is to study the effect of the flapping radius, this is the only parameter that varies. The rest of the parameters are set to be equal to the ones of § 5.2. Hence, the reduced frequency is $k = 1$; the maximum amplitude of the wing tips is $h_{0_t} = 1c$; the aspect ratio of the wings is $AR = 2$ and the distance between them when both are parallel is $d = 0.5c$. The wings are moving with a forward velocity U_∞. Each wing is discretized into $i_N = 4$ and $j_N = 15$ panels. The analysed flapping radii are: $R = [2c, 2.25c, 2.5c, 5c, 10c]$. The physical meaning of the flapping radius is sketched in Figure 5.6. Only the right wing is sketched, but the same applies to the left wing.

The reference frame of each wing has been chosen to coincide when the flapping angle, φ, is 0. Therefore, in Figure 5.6, $y_t = 2.25c$. For the right wing, the kinematics of the motion turns out to be:

$$X^I_{O_R}(t) = -U_\infty, \quad Y^I_{O_R}(t) = (R - y_t)(\cos\varphi - 1), \quad Z^I_{O_R}(t) = (R - y_t)\sin\varphi,$$

$$\varphi_R(t) = \varphi_0 \sin\omega t, \qquad \theta_R(t) = 0, \qquad \psi_R(t) = 0.$$

For the left wing, same equations apply, but $Y_{O_L} = -Y_{O_R}$ and $\varphi_L = -\varphi_R$. The flapping amplitude, from Figure 5.6, is $\varphi_0 = \sin^{-1}(h_{0_t}/R)$.

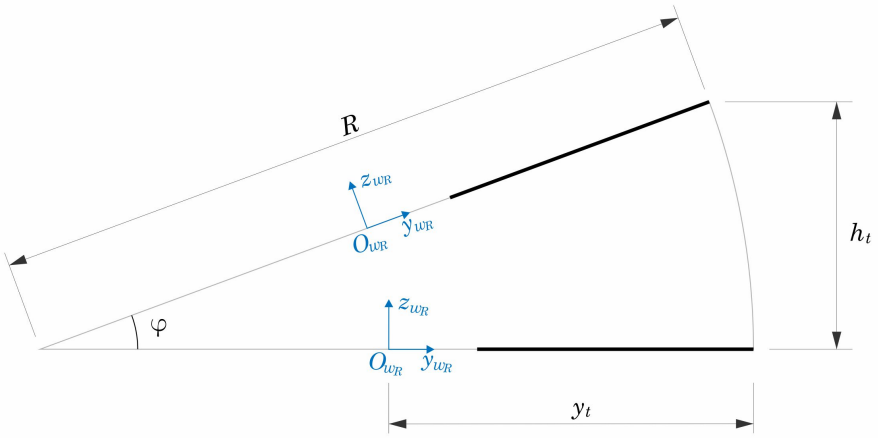

Figure 5.6: Description of flapping motion parameters.

5.3.1 Aerodynamic Forces and Pressure distribution

Normal and tangential forces are displayed in Figure 5.7. The case with $R = \infty$ corresponds to a pure heaving oscillation. In a first instance, it is highlighted the behaviour of the forces is similar to a heaving motion. In Figure 5.7a, the normal forces are sketched. It can be observed that the net normal force increases as the flapping radius increases and is always lower than the force produced under a heaving motion. The same behaviour is observed for the tangential forces, sketched in Figure 5.7b.

The decrease in the forces as R is reduced can be explained as follows. While in heaving, all the points of the wing have the same velocity; in flapping, the velocity of the wing's points is proportional to the distance from the flapping centre. Therefore, points nearest to the root, have a lower velocity; and in turn, the pressure difference at these points is lower. In order to get a better insight, the force distribution along the wing is studied. Particularly, it is interesting to know the force distribution along the span; thus, the force per unit span, $F'(y)$, is depicted in Figure 5.8 (right wing). It can be appreciated, on the one hand, that the asymmetric force distribution is more pronounced in the wings with a lower flapping radius. On the other hand, regardless of the pressure distribution, the force per unit span at a given point is higher for higher flapping radii.

5.3.2 Propulsive Efficiency

From the previous discussion, one can infer a pure heaving motion –or a flapping motion with a high R– is preferable since more force is generated. However, heaving

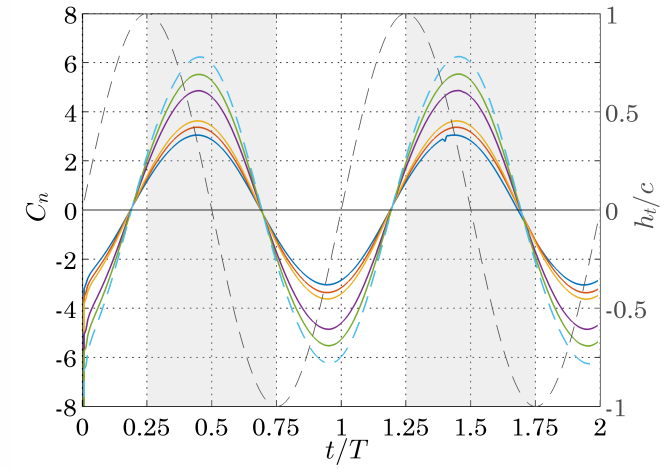

(a) Normal Force

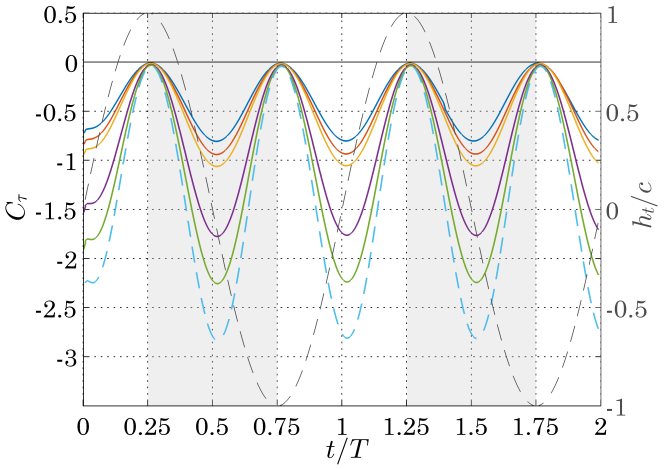

(b) Tangential Force

Figure 5.7: Force Coefficients vs. non dimensional time (Flapping Motion). (—) $R = 2c$; (—) $R = 2.25c$; (—) $R = 2.5c$; (—) $R = 5c$; (—) $R = 10c$; (- - -) $R = \infty$.

motion could entail higher power requirements to move the wings and generate the desired motion. In order to assess this, the propulsive efficiency is used.

The propulsive efficiency is usually defined as the ratio between the mean thrust coefficient and the mean power coefficient (see eq. (5.2)). The power coefficient is the nondimensional power required to move the wings. Therefore, the propulsion efficiency serves to relate the thrust that is generated to the power that is required to generate such thrust.

$$\eta_p = \frac{-\overline{C_\tau}}{\overline{C_p}} \tag{5.2}$$

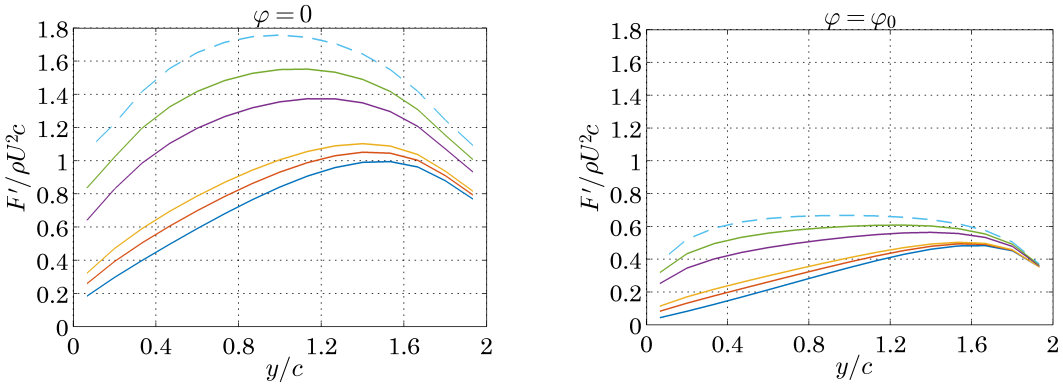

(a) $\varphi = 0$ (Downstroke). **(b)** $\varphi = \varphi_0$.

Figure 5.8: Force per unit span at two different instants (right wing). (—) $R = 2c$; (—) $R = 2.25c$; (—) $R = 2.5c$; (—) $R = 5c$; (—) $R = 10c$; (- - -) $R = \infty$.

As appreciated in § 5.2, the results of *AeroFlaps* correspond to a case where viscous effects (separation and skin friction) are absent. As such, one must be careful when extrapolating the results presented below to real cases.

In order to estimate the required power to each configuration, the power is calculated as defined in eq. (5.3).

$$P = \boldsymbol{M}_{O_w} \cdot \boldsymbol{\Omega} + \boldsymbol{F} \cdot \boldsymbol{V}_{O_w} \tag{5.3}$$

In eq. (5.3), $\boldsymbol{M}_{O_w}$ is the moment about the origin of the wing's reference frame, and $\boldsymbol{F}$ are the aerodynamic forces. The power is nondimensionalized according to:

$$C_p = \frac{P}{\frac{1}{2}\rho S U_\infty^3}$$

The nondimensional power is depicted in Figure 5.9. Results are obtained for the right wing, but a similar result is obtained for the left wing. In the figure, negative power means that in order to produce the given motion, power has to be supplied. As one could expect, required power is higher at instants when higher forces are developed. Moreover, one can appreciate that the required power increases as the flapping radius increases, since more force is produced.

Propulsive efficiencies, as well as mean values of C_τ and C_p for a single period are gathered in Table 5.1 (in accordance to eq. (5.2), C_p is positive when it refers to required power).

In Table 5.1 one can appreciate η_p initially increases with the flapping radius, but for $R > 5c$, it slightly decreases. Therefore, for the present wings' configuration,

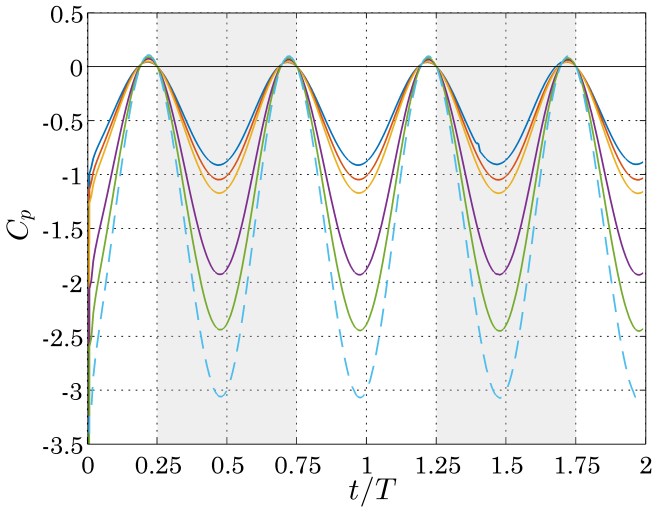

Figure 5.9: Power coefficient vs. nondimensional time. (—) $R = 2c$; (—) $R = 2.25c$; (—) $R = 2.5c$; (—) $R = 5c$; (—) $R = 10c$; (- - -) $R = \infty$.

	Flapping Radius, R						
	$2c$	$2.25c$	$2.5c$	$3.5c$	5	$10c$	∞
$\overline{C_n}$	0.966	1.092	1.177	1.308	1.580	1.800	2.032
$-\overline{C_\tau}$	0.205	0.237	0.268	0.320	0.448	0.568	0.710
$\overline{C_p}$	0.435	0.503	0.563	0.666	0.929	1.181	1.480
η_p	0.470	0.472	0.477	0.481	0.482	0.481	0.479
$-\overline{C_n}/\overline{C_t}$	4.721	4.602	4.393	4.085	3.527	3.169	2.864

Table 5.1: Propulsive efficiency for different flapping radii.

and being always conservative with the results, the highest propulsive efficiency is reached for flapping radii near $5c$.

In order to go in depth in the study, an additional estimation of the efficiency is obtained by measuring the ratio of lift to thrust. In Figure 5.7a, it is noted the mean value of the normal force is 0. Thus, contrary to previous estimation, mean value of C_n is computed in the interval where $C_n > 0$. The results are also gathered in Table 5.1.

From Table 5.1, one can appreciate that the ratio of normal to tangential forces is higher for decreasing flapping radius, hence a heaving motion produces a higher thrust to lift ratio than a flapping motion. Note that in this case there is no minimum value like in the previous comparison. This difference between the propulsive efficieny and the "aerodynamic" efficiency suggests that the distribution of forces

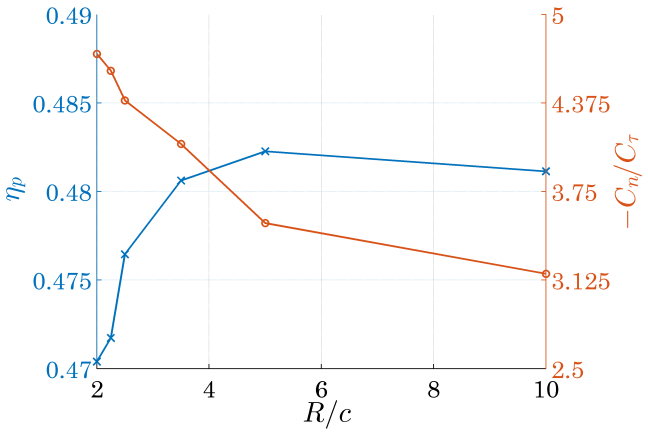

Figure 5.10: Efficiencies vs. flapping radius.

along the wing plays an important role in the required power –Recall that, from eq. (5.3), the required power is formed by two terms, one related to total force, and another related to force distribution (moments). As a consequence, a flapping motion with a radius of $5c$ seems to be optimal not due to a higher thrust to lift ratio, but due to a better force distribution along the span of the wings. The efficiencies gathered in Table 5.1 are displayed in Figure 5.10.

To conclude with, it must be highlighted this study is limited; and more advanced studies should be performed. Studies of interest could be focused on the effect of the reduced frequency; likewise, *flapping-pitching* configurations producing a net lift and thrust should be studied and their corresponding efficiencies, analysed.

Chapter 6

Conclusions and Future Research

6.1 Summary

In the present project, an unsteady potential aerodynamic code (named *AeroFlaps*) to model a pair of flapping wing has been developed. The main objective was to compute the aerodynamic forces produced by an imposed wing motion. To develop the aerodynamic model, wings have been assumed to be infinitely thin surfaces and vortex-rings have been bound to them to simulate wings' circulation. The wake left by the wings has also been modelled using vortex-ring elements which are free to move with the fluid velocity.

As a first step, a simplified version of the code (named *OneWing*) with a single wing has been developed too. This code has been directly validated with the results from [16]; and the final algorithm has been validated with this simplified version. Besides, heaving and flapping cases with a high stroke amplitude have been run and the results have been analysed and compared to the ones of a high order NS model. It has been observed that normal forces on the wings are accurately predicted using the code. On the other hand, from the potential approach, viscous effects are not included in tangential forces. It has been observed that skin friction and boundary layer separation contribute significantly to these forces due to the high heaving amplitude and the low Reynolds regime at which the simulation is performed. A better approach to compute tangential forces is envisaged as a future task.

A preliminary study of different flapping regimes was performed. In this study, different flapping radii were analysed and the results were compared. In terms of lift production, it was observed that under the same flapping amplitude, two wings in pure heaving produced a higher lift coefficient. Moreover, propulsive efficiency

was also analysed. In this case, it was appreciated a maximum propulsive efficiency is obtained at a given radius. Deeper studies must be performed in this area.

In a different research line, *OneWing* was modified and implemented inside a dynamic model to simulate a free flight of a flapping wing MAV. In this line, *AeroFlaps* will also be modified to allow further studies concerning this area, such as asymmetric flight configurations.

6.2 Future Research

Several tasks can be done to continue with the research line presented in this document. They can be grouped into two main groups. On the one hand, several improvements could be performed aimed to complete the algorithm. Although it has been demonstrated that the present code accurately predicts normal forces associated to pressure differences, several contributions to tangential forces are not accounted for in the model. In order to solve this, several improvements on the potential code can be made:

- Modelling of wings with thickness and rounded marginal edges. Avoiding infinitely thin surfaces, suction forces at the edges can be computed correctly.
- Boundary layer separation. It is possible to simulate boundary layer separation in a potential code by detaching vortex-ring elements at the separation point. However, determining the separation point and the vortex ring strength is difficult. In fact, most potential codes that includes separation are based on empirical data. Therefore, a research line is the development of a model that reasonably predicts boundary layer separation in a potential flow. A possible model could be based on computing pressure gradients on the wing.
- Skin friction. Skin friction is an important contributor to drag force; therefore, it would be advisable to somehow estimate its contribution to the tangential forces.

The model can also be improved by taking into account wings' flexibility. Animals' wings are not rigid, but they deform under aerodynamic loads changing its shape. In fact, wing deformation has an important role in the production of aerodynamic forces [28]. Wing's flexibility can be simulated considering the wing as a structural model, for example, as a isotropic flat plate, as a shell, *etc* (see [1]).

On the other hand, deeper analyses of wings in flapping motion should be assessed. The present study has been restricted to the effect of flapping radius. Thus, a wider study on the effect of different flapping wing parameters should be made. An study

focused on the effect of the reduced frequency on the forces sounds promising. Furthermore, combinations of pitching and flapping motions that produces both mean lift and thrust should be investigated.

Appendix A

Induced velocity by a Contant-Strength Vortex Ring

In this Appendix, the analytical formula implemented in the algorithm to compute the induced velocity by a vortex ring is presented. The procedure followed is similar to the one originally explained in [29].

In Chapter 3 the analytic expression to compute the induced velocity by a constant strength vortex segment was presented. This equation is derived from the Biot-Savart law (see Section 2.11 of [16]) and is written below as appearing in § 3.4.

$$\nabla\phi(\boldsymbol{x}_p) = \frac{\Gamma}{4\pi}\oint_C \frac{d\boldsymbol{l}\times\boldsymbol{r}}{r^3} \tag{3.56}$$

In order to implement eq. (3.56) in an algorithm, the first option is to split the integral into the addition of small elements. This process entails a high computing time, taking into account that it must be repeated for each vortex ring and at every time step. Fortunately, an analytical solution to eq. (3.56) when the line integral is a straight segment can be obtained. Therefore, a vortex line can be split into 4 straight segments, and the total induced velocity by the vortex ring at a given point is the contribution of the four segments.

A.1 Induced velocity by a Constant-Strength Vortex straight segment

In Figure A.1 a vortex segment with known vortex strength Γ is sketched. Thus, according to eq. (3.56), the induced velocity by the segment at a point P is:

$$\boldsymbol{v}_P = \frac{\Gamma}{4\pi} \int_1^2 \frac{d\boldsymbol{l} \times \boldsymbol{r}}{r^3} \tag{A.1}$$

From eq. (A.1), one can infer that $\boldsymbol{v}_P$ is perpendicular to the plane in which both $d\boldsymbol{l}$ and $\boldsymbol{r}$ are contained. Therefore, eq. (A.1) can be rewritten in the following way:

$$v_P = \frac{\Gamma}{4\pi} \int_1^2 \frac{\sin\beta}{r^2}\, dl. \tag{A.2}$$

From Figure A.1 it can be worked out that:

$$r = \frac{d}{\sin\beta}, \qquad\qquad l = -\frac{d}{\tan\beta}.$$

Therefore,

$$dl = \frac{d}{\sin^2\beta}$$

Upon substitution of the previous terms into eq. (A.2):

$$v_P = \frac{\Gamma}{4\pi} \int_{\beta_1}^{\beta_2} \frac{\sin\beta}{d}\, d\beta \tag{A.3}$$

As it can be appreciated in Figure A.1, d is constant for a straight segment; thus, it can be taken out of the integral. Finally, the induced velocity can be computed as:

$$v_P = \frac{\Gamma}{4\pi d} \int_{\beta_1}^{\beta_2} \sin\beta\, d\beta = \frac{\Gamma}{4\pi d}(\cos\beta_1 - \cos\beta_2) \tag{A.4}$$

However, for the developed algorithm in MATLAB® it is easier to work with vectors rather than angles. Therefore, eq. (A.4) can be rewritten using vector notation. Defining $\boldsymbol{r}_0 = \boldsymbol{r}_1 - \boldsymbol{r}_2$ and noting that:

$$\cos\beta_1 = \frac{\boldsymbol{r}_1 \cdot \boldsymbol{r}_0}{r_1 r_0}, \qquad\qquad \cos\beta_2 = \frac{\boldsymbol{r}_2 \cdot \boldsymbol{r}_0}{r_2 r_0}$$

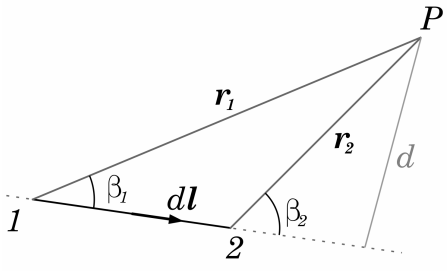

Figure A.1: Definition of the vectors and angles for the velocity induced by a straight segment

and

$$d = r_1 \sin\beta_1 = r_1 \frac{\|\boldsymbol{r}_0 \times \boldsymbol{r}_1\|}{r_0 r_1} = \frac{\|\boldsymbol{r}_1 \times \boldsymbol{r}_2\|}{r_0},$$

eq. (A.4) becomes:

$$v_P = \frac{\Gamma}{4\pi} \frac{\boldsymbol{r_0}}{\|\boldsymbol{r}_1 \times \boldsymbol{r}_2\|} \left(\frac{\boldsymbol{r}_1}{r_1} - \frac{\boldsymbol{r}_2}{r_2} \right) \tag{A.5}$$

The unit direction of v_P is given by the unit vector $\boldsymbol{n} = (\boldsymbol{r}_1 \times \boldsymbol{r}_2)/\|\boldsymbol{r}_1 \times \boldsymbol{r}_2\|$. Hence:

$$\boldsymbol{v}_P = \frac{\Gamma}{4\pi} \frac{\boldsymbol{r}_1 \times \boldsymbol{r}_2}{\|\boldsymbol{r}_1 \times \boldsymbol{r}_2\|^2} \boldsymbol{r_0} \left(\frac{\boldsymbol{r}_1}{r_1} - \frac{\boldsymbol{r}_2}{r_2} \right) \tag{A.6}$$

In the previous development the notation $r = \|\boldsymbol{r}\|$ has been used. By looking at eq. (A.6), one can note that if P is very close to the segment $1-2$, $\boldsymbol{v}_P$ tends to infinity. Due to the continuous wake *roll-up*, a wake element is prone to get too close to another wake element and due to eq. (A.6), is displaced a great distance from one time step to the next. It should be highlighted that this troublesome behaviour is found in potential flow only, since viscous effects are not present. This undesirable effect can be overcome by the addition of a *cut-off radius parameter*, δ, following the approach in [22]. In this fashion, eq. (A.6) is modified as follows:

$$\boldsymbol{v}_P = \frac{\Gamma}{4\pi} \frac{\boldsymbol{r}_1 \times \boldsymbol{r}_2}{\|\boldsymbol{r}_1 \times \boldsymbol{r}_2\|^2 + (\delta d_m)^2} \boldsymbol{r_0} \left(\frac{\boldsymbol{r}_1}{r_1} - \frac{\boldsymbol{r}_2}{r_2} \right) \tag{A.7}$$

Now, when P approaches the vortex segment, velocity smoothly tends to zero. In eq. (A.7), d_m is the shortest distance of a vortex ring; thus, it is defined as $d_m = \Delta t U_c$. On the other hand, δ is an arbitrary constant from 0 to 1. Its effect on the induced velocity is depicted in Figure A.2. For the developed algorithm, $\delta = 0.01$.

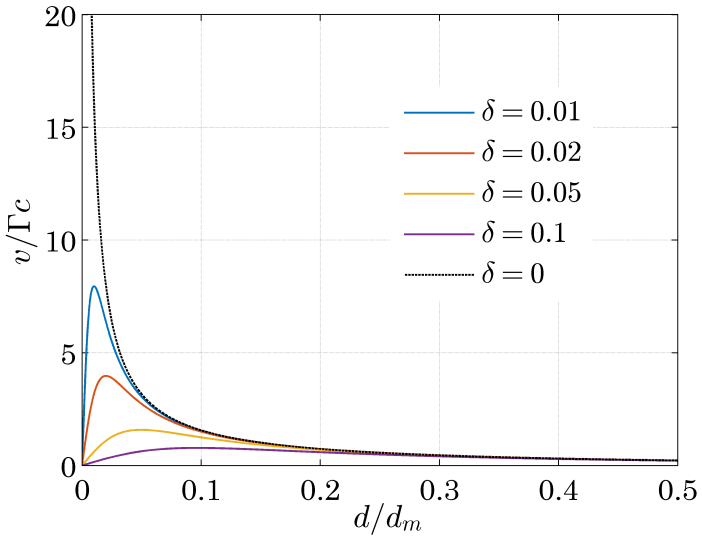

Figure A.2: Effect of the *cut-off radius* on the induced velocity. d is the perpendicular distance of the point to the vortex segment, and the point is located equidistant to both segment ends.

Appendix B

Project Budget

In this appendix, an estimation of the project budget is presented. The main items are detailed below:

- **Laptop**. In order to develop the codes and validate them, a laptop was required. It is an Intel Core i3-370M, *acer* computer priced at 600 €.
- **Matlab® License**. MATLAB® has been used both for both code development of and post-processing analysis. A MATLAB® academic license is priced at 500 €.
- **Labour hours**. The salary of a junior engineer in a research project is estimated to be 25 €/h. The hours needed to complete the project are estimated to be 600 h. Thus, the total cost is 15,000 €.
- **Computing hours**. Although computations can be performed using a laptop, for long time simulations, laptop RAM does not have enough space. For that reason, an HPCC[1] is used. An estimation based on Spanish CESGA center yields a price of 0.2 € per computing hour and processor. It is estimated that 20 h using 1 processor have been required for the entire project. Thus, total computing cost is 4 €.

[1] HPCC stands for High-Performance Computing Cluster

Project cost is summarized in Table B.1.

Item	Price €
Laptop	600
MATLAB® license	500
Labour hours	15,000
Computing hours	4
Total	**16,104**

Table B.1: Project budget

Bibliography

[1] W. (Wei) Shyy. *An introduction to flapping wing aerodynamics*. Cambridge University Press, Cambridge [etc.], 2013.

[2] Luca Petricca, Per Ohlckers, and Christopher Grinde. Micro- and nano-air vehicles: State of the art. *International journal of aerospace engineering*, 2011(4):1; 1–17; 17, 2011. doi: 10.1155/2011/214549 pmid:.

[3] C. Galiński and R. Zbikowski. Some problems of micro air vehicles development. *Bulletin of the Polish Academy of Sciences: Technical Sciences*, 55(1):91–98, 2007.

[4] C. De Wagter, S. Tijmons, B. D. W. Remes, and G. C. H. E. de Croon. Autonomous flight of a 20-gram flapping wing mav with a 4-gram onboard stereo vision system. In *Robotics and Automation (ICRA), 2014 IEEE International Conference on*, pages 4982–4987, 2014. ID: 1.

[5] Kevin Y. Ma, Pakpong Chirarattananon, Sawyer B. Fuller, and Robert J. Wood. Controlled flight of a biologically inspired, insect-scale robot. *Science*, 340(6132):603–607, 2013.

[6] Matthew Keennon, Karl Klingebiel, Henry Won, and Alexander Andriukov. Development of the nano hummingbird: A tailless flapping wing micro air vehicle. 2012.

[7] Peng Chai and David Millard. Flight and size constraints: Hovering performance of large hummingbirds under maximal loading. *Journal of Experimental Biology*, 200(21):2757–2763, 1997.

[8] Steven N. Fry, Rosalyn Sayaman, and Michael H. Dickinson. The aerodynamics of hovering flight in drosophila. *Journal of Experimental Biology*, 208(12):2303–2318, 2005.

[9] R. Dudley and C. P. Ellington. Mechanics of forward flight in bumblebees. *Journal of Experimental Biology*, 148:53–88, 1990.

[10] Sanjay P. Sane. The aerodynamics of insect flight. *Journal of Experimental Biology*, 206(23):4191–4208, 2003.

[11] MJC Smith, PJ Wilkin, and MH Williams. The advantages of an unsteady panel method in modelling the aerodynamic forces on rigid flapping wings. *Journal of Experimental Biology*, 199(5):1073–1083, 1996.

[12] P. O Persson, D. J. Willis, and J. Peraire. Numerical simulation of flapping wings using a panel method and a high-order navier-stokes solver. *International Journal for Numerical Methods in Engineering*, 89(10):1296–1316, 2012.

[13] Uav drone market for commercial worth $ 1.27 billion by 2020. *PR Newswire Europe Including UK Disclose*, 2015.

[14] Spain. Ley orgánica 18/2014, 15 de octubre, de aprobación de medidas urgentes para el crecimiento, la competitividad y la eficiencia. *BOE*, 252:52544–52715, October 2014.

[15] Blanca Martínez Gallar. Dynamic models for flapping-wing micro-air vehicles, 2015.

[16] Joseph (1947-). Katz and Allen Plotkin. *Low speed aerodynamics*, volume 13. Cambridge University Press, Cambridge [etc.], 2001.

[17] Antonio L. Sánchez and Javier Rodríguez-Rodríguez. *Fluid Mechanics: An introduction and some relevant applications*. 2011.

[18] K. Suzuki, K. Minami, and T. Inamuro. Lift and thrust generation by a butterfly-like flapping wing-body model: immersed boundary-lattice boltzmann simulations. *Journal of Fluid Mechanics*, 767:659–695, 2015.

[19] Mark Drela. *Flight vehicle aerodynamics*. MIT Press, Cambridge, 2014.

[20] Tracy E. Fritz and Lyle N. Long. Object-oriented unsteady vortex lattice method for flapping flight. *Journal of Aircraft*, 41(6):1275–1290, 2004.

[21] P. G. Saffman. *Vortex dynamics*. Cambridge University Press, Cambridge, 1992; 1993.

[22] Bruno A. Roccia, Sergio Preidikman, Julio C. Massa, and Dean T. Mook. Modified unsteady vortex-lattice method to study flapping wings in hover flight. *AIAA Journal*, 51(11):2628–2642, 2013.

[23] F. Edward Ehlers and Marjorie E. Manro. A method for computing the leading-edge suction in a higher-order panel method. Technical Report NASA-CR-3730, 1984.

[24] J. Katz. Calculation of the aerodynamic forces on automotive lifting surfaces. *Journal of Fluids Engineering*, 107(4):438–443, December 1 1985.

[25] Rafael Fernández Prats et al. Hydrodynamics of a pitching foils: flexibility and ground effects. 2015.

[26] Ratnesh K. Shukla and Jeff D. Eldredge. An inviscid model for vortex shedding from a deforming body. *Theoretical and Computational Fluid Dynamics*, 21(5):343–368, 2007.

[27] Abhijit Gogulapati and Peretz P. Friedmann. Approximate aerodynamic and aeroelastic modeling of flapping wings in hover and forward flight. 2011.

[28] Liang Zhao, Qingfeng Huang, Xinyan Deng, and S. Sane. The effect of chordwise flexibility on the aerodynamic force generation of flapping wings: Experimental studies. pages 4207–4212, 2009.

[29] A. Robinson and J.A. Laurmann. *Wing theory*. Cambridge aeronautical series. University Press, 1956.